

ALMA Central molecular zone Exploration Survey (ACES) V: CS(2 – 1), SO(2₃ – 1₂), CH₃CHO(5_{1,4} – 4_{1,3}), HC₃N(11 – 10) and H40 α lines data

Pei-Ying Hsieh,^{1*} Daniel. L. Walker,² Adam Ginsburg,³ Ashley T. Barnes,⁴ Xing Lu,^{5,6} Álvaro Sánchez-Monge,^{7,8} Savannah R. Gramze,³ Nazar Budaiev,³ Marc W. Pound,⁹ Jaime E. Pineda,¹⁰ Claire Cook,¹¹ Jonathan D. Henshaw,^{12,13} Katharina Immer,⁴ Namitha Issac,⁵ Desmond Jeff,³ Fu-Heng Liang,^{14,4} Steven N. Longmore,^{12,15} Elisabeth A.C. Mills,¹¹ Sergio Martín,^{16,17} Xing Pan,^{18,19,20} Thushara G.S. Pillai,²¹ Qizhou Zhang,²⁰ John Bally,²² Cara Battersby,²³ Laura Colzi,²⁴ Paul T. P. Ho,²⁵ Izaskun Jiménez-Serra,²⁴ J. M. Diederik Kruijssen,¹⁵ Maya Petkova,²⁶ Mattia C. Sormani,²⁷ Robin G. Tress,²⁸ Jennifer Wallace,²³ J. Armijos-Abendaño,²⁹ Lucia Armillotta,³⁰ N. Bijas,³¹ Rojita Buddhacharya,¹² Laura A. Busch,¹⁰ Natalie O. Butterfield,³² Mélanie Chevance,^{33,15} Ana Karla Díaz-Rodríguez,² Christoph Federrath,³⁴ Rubén Fedriani,³⁵ Pablo García,^{36,37} Qi-Lao Gu,⁵ Rebecca J. Houghton,¹² Yue Hu,³⁸ Janik Karoly,³⁹ Ralf S. Klessen,^{33,40,20,41} Mark R. Krumholz,³⁴ Farideh Mazoochi,⁴² Francisco Nogueras-Lara,^{35,4} Dylan Paré,⁴³ Denise Riquelme-Vásquez,⁴⁴ Víctor M. Rivilla,²⁴ Miriam G. Santa-Maria,^{3,45} Anika Schmiedeke,⁴⁶ Yoshiaki Sofue,⁴⁷ Volker Tolls,²⁰ Q. Daniel Wang,⁴⁸ Gwenllian M. Williams,⁴⁹ Fengwei Xu,^{50,51} and Suinan Zhang⁵

* Author affiliations are listed at the end of the paper

3 March 2026

ABSTRACT

We present data from the ALMA Central Molecular Zone Exploration Survey (ACES) Large Program, which provides broad spectral-line and 3 mm continuum coverage of the Central Molecular Zone (CMZ) at a spatial resolution of 0.1 pc. The survey delivers homogeneous, wide-field mosaics that enable direct comparisons of the physical and chemical conditions across diverse environments in the Galactic center. In this data release paper, we present the CS(2 – 1), SO(2₃ – 1₂), CH₃CHO(5_{1,4} – 4_{1,3}), HC₃N(11 – 10), and H40 α lines observed simultaneously within two broad spectral windows. These lines reveal pronounced spatial and chemical variations across the CMZ, tracing distinct components of molecular gas, shock-affected regions, and ionized structures. The high angular resolution and multi-line capability of the ACES dataset make it a powerful resource for future studies of gas dynamics, star formation activity, and the physical connection between the CMZ and Sgr A*.

Key words: Galaxy: centre < The Galaxy, ISM: structure < Interstellar Medium (ISM), Nebulae

1 INTRODUCTION

The central molecular zone (CMZ) is a dense reservoir of molecular gas within the innermost ~ 300 pc of the Galactic center (GC), confined to a vertically thin disk with a scale height of 30–50 pc. The total gas mass is estimated at $\sim (5\text{--}10) \times 10^7 M_{\odot}$, accounting for roughly 10% of the Milky Way’s molecular gas (Morris & Serabyn 1996; Genzel et al. 2010, and references therein). Most of this mass is concentrated in compact giant molecular clouds (GMCs) with typical

masses of $10^{5.5}$ to $10^{6.5} M_{\odot}$. Hence, the large volume of molecular gas makes it an excellent environment for star formation.

Molecular gas in the CMZ exhibits physical conditions distinct from those in the Galactic disk. The CO-to-H₂ conversion factors and gas surface densities in the CMZ resemble those found in starburst galaxies (see Figure 10 in Tacconi et al. 2008). The gas has high temperatures, turbulence, and pressure (Ao et al. 2013; Mills et al. 2013; Ginsburg et al. 2016; Immer et al. 2016), sharing characteristics with active star-forming regions in many different extragalactic environments (Kruijssen & Longmore 2013). However, despite the presence of dense gas, the current star formation rate (SFR) in the

* E-mail: pei-ying.hsieh@nao.ac.jp

CMZ is only $\sim 10\%$ of what is expected from standard dense gas–SFR scaling relations (Longmore et al. 2013; Barnes et al. 2017; Lu et al. 2019a; Henshaw et al. 2023). Understanding how these physical conditions are related to the suppressed star formation in the CMZ requires further observational and theoretical studies which link the global gas properties to the sub-parsec scales at which star formation occurs (Kruijssen et al. 2014, 2019; Krumholz & Kruijssen 2015; Krumholz et al. 2017; Tress et al. 2020; Sormani et al. 2022).

The Atacama Large Millimeter/submillimeter Array (ALMA) CMZ Exploration Survey (ACES) Large Program (Longmore & ACES Team 2025, project code: 2021.1.00172.L; PI: S. Longmore; hereafter Paper I) provides uniform Band 3 coverage of the inner $1.5^\circ \times 0.5^\circ$ of the CMZ, producing the largest mosaic yet made with ALMA and achieving an unprecedented angular resolution of $\sim 2''$ in both spectral-line and continuum emission. This new global, high-resolution and sensitivity view of the physical, kinematic and chemical structure facilitates ACES main science objective to build a global understanding of star formation, feedback, and the mass flows and energy cycles across the Central Molecular Zone. ACES employed 6 spectral windows to span a wide range of frequency coverage. The continuum dataset, covering an effective bandwidth of 4.6 GHz, is described in detail by Ginsburg & ACES Team (2025). The high-resolution spectral-line data and details of the data combination will be presented by Walker & ACES Team (2025), while the intermediate-resolution spectral-line data will be presented by Lu (2025). In this paper, we present the data release of two broadband spectral windows that include the lines of CS(2 – 1) (carbon monosulfide), SO(2₃ – 1₂) (sulfur monoxide), HC₃N(11 – 10) (cyanoacetylene), CH₃CHO(5_{1,4} – 4_{1,3}) (acetaldehyde), and the radio recombination line H40 α . The characteristics of these lines are summarized in Table 1.

2 OBSERVATIONS AND DATA PROCESSING

Forty-five individual mosaics were used to image the central $1.5^\circ \times 0.5^\circ$ of the CMZ with the ALMA Band 3 receiver and the 12-m array. The 7-m and TP arrays were also employed to recover the short-spacing information. The overall survey design and observational setup are described in Longmore & ACES Team (2025, hereafter Paper I), while details of the data calibration and imaging procedures are given in Ginsburg & ACES Team (2025); Walker & ACES Team (2025, hereafter Paper II; Paper III). The data product releases of the continuum and spectral-line cubes are presented in Paper II, Paper III, Lu (2025, hereafter Paper IV), and in this work.

We use the CASA package (CASA Team et al. 2022) for calibration and imaging. The majority of the data were processed with CASA version 6.2.1.7 and version 6.4.1.12 for the later dataset, as the project extended across different observing cycles and pipeline version releases. The full details of the CASA versions used can be found in Paper II. In this paper we present the spectral cubes of the broad spectral windows (SPW 33 and SPW 35 in Table 1 of Paper III). The spectrum of broad spectral window towards the water maser core of the Brick cloud is shown in Figure 1. The conversion factors from Jy beam⁻¹ to K are 21.2, 20.7, 23.4, and 20.8 for CS(2 – 1), SO(2₃ – 1₂), HC₃N(11 – 10) and CH₃CHO(5_{1,4} – 4_{1,3}), respectively. Detailed descriptions of the data issues, continuum subtraction, deconvolution (image reconstruction), array combination, and mosaic procedures

are provided in Paper III and in the `merge_tclean_commands.py` script in the ACES GitHub repository¹.

The CASA task `feather` was used to combine the images from the 12 m, 7 m, and TP arrays for the data release. Section 3.5 of Paper III provides a detailed discussion of various array combination methods using CASA. In this work, we adopted the “feather-only” approach as described in Section 3.5.3 of Paper III. Additionally, Paper IV discussed alternative combination methods using Miriad (Sault et al. 1995). The native channel width of the broad spectral window is 1.48 km s⁻¹ with an effective bandwidth of ~ 1.86 GHz (~ 5680 km s⁻¹). The image rms noise per 1.48 km s⁻¹ channel is not uniform across the mosaics, but varies between regions typically in the range of 3–5 mJy beam⁻¹. The cube statistics are shown in Table C1. The id of each field can also be found in Paper III and Paper II. For the purpose of mosaic, image cubes of individual fields were smoothed to a common beam to produce the final, full-CMZ mosaics. The common beam size is applied to the mosaic maps, while most of the individual fields have high angular resolution, the final beam is compromised with the lowest resolution of field am. The common beam sizes of the SPW 33 and SPW 35 are $2.84'' \times 2.11''$ (position angle= -89.46°) and $2.65'' \times 1.97''$ (position angle= -89.96°), respectively.

We compare the ACES CS(2 – 1) data with the NRO 45 m CS(2 – 1) data (Hsieh et al. 2016). The spatial and spectral resolutions of the 45 m data are $38''$ and 2.5 km s⁻¹, respectively. The total bandwidth of the 45 m data is 400 km s⁻¹, which is narrower than that of the ACES data. The 45 m image was obtained in units of T_A^* , and we converted it to T_B by dividing by the main-beam efficiency of 0.43 (Hsieh et al. 2016). To compare with the ACES map, we generated `mom0` maps for both datasets using the same method described in Section 3.1, integrating over the same velocity range and smoothing to a common beam size of $38''$. The ratio image is shown in Figure 2. The mean ratio across the masked region is approximately 0.9, indicating that our flux calibration is consistent with the 45 m data. Elevated ratios near Sgr C may be affected by edge effects in the maps, while the high values near Sgr A* are likely due to residual continuum emission in the ACES data.

3 ACES DATA PRODUCTS AND STRUCTURAL HIGHLIGHTS

3.1 Moment Maps of CMZ Mosaics

We present the integrated intensity (`mom0`) and peak intensity (`mom8`) mosaic images (a nomenclature within the `immoments` task of CASA) of these four molecular lines in Figure 3, Figure 4 and Figure 5. The zoomed-in images of H40 α are presented in Figure A1.

Note that the CH₃CHO(5_{1,4} – 4_{1,3}) `mom0` map includes both the CH₃CHO(5_{1,4} – 4_{1,3}) E and CH₃CHO(5_{1,4} – 4_{1,3}) A transitions to improve the signal-to-noise ratio. These two lines are close in frequency, separated by approximately ± 150 km s⁻¹. If high-velocity components (e.g., ± 150 km s⁻¹), such as those from the circumnuclear disk (CND) are present, the lines may become spectrally blended in our data. However, since the CND is not clearly detected in either transition, the CH₃CHO(5_{1,4} – 4_{1,3}) `mom0` map shown in Figure 3 is not affected by blending from high-velocity components. Users can generate individual `mom0` maps for each transition directly from the mosaic cube. Details on generating moment maps can be found in Paper III.

¹ https://github.com/ACES-CMZ/reduction_ACES

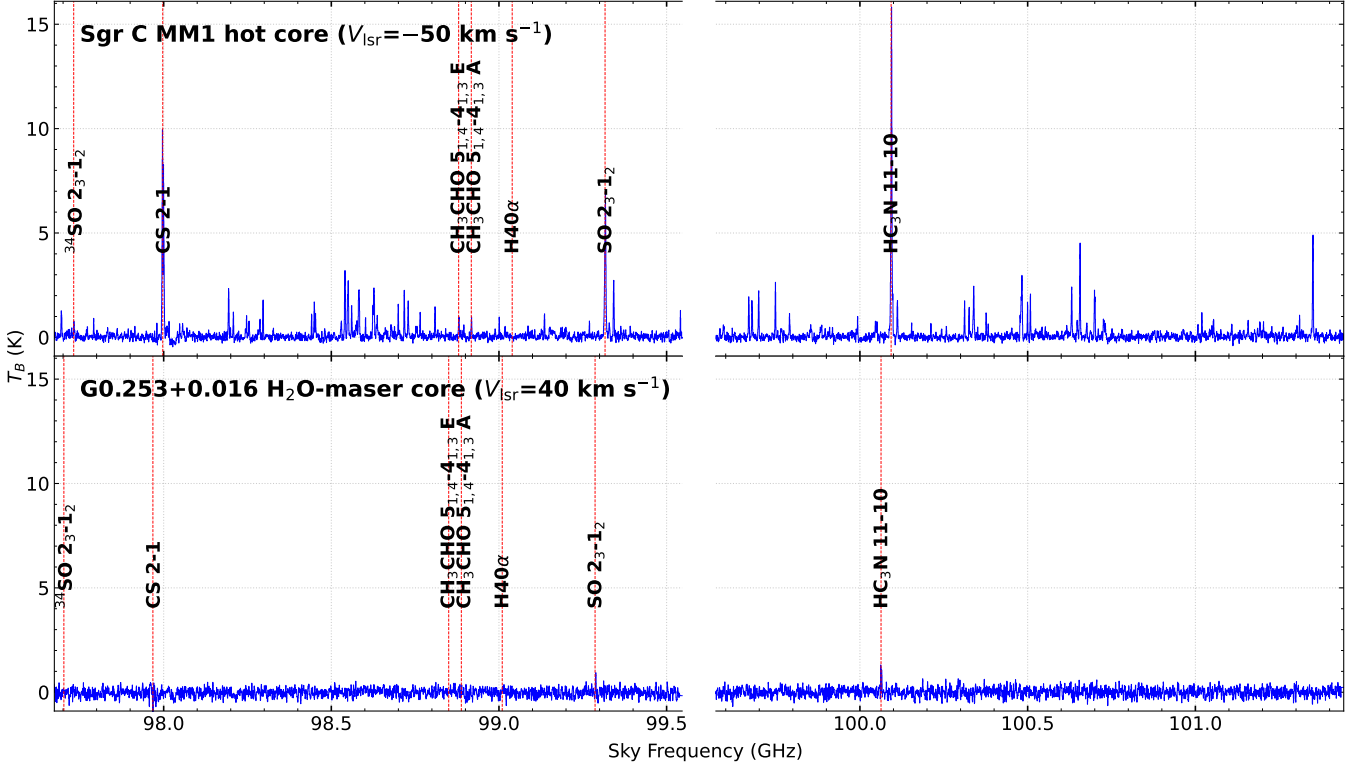


Figure 1. The spectra of broad spectral windows (SPW 33, 35) towards the Sgr C MM1 hot core and water maser core of Brick cloud. The lines presented in this paper are labeled. The native channel width of broad spectral window is 1.48 km s^{-1} with an effective bandwidth of $\sim 1.86 \text{ GHz}$ ($\sim 5680 \text{ km s}^{-1}$ per spectral window).

Table 1. Key lines covered by the broadband spectral windows.

Lines	Rest frequency (GHz)	A_{ul} s^{-1}	E_u/k (K)	n_{crit}^a (cm^{-3})
CS(2 – 1)	97.98095	1.679E-5	7.1	2.8×10^5
SO($2_3 - 1_2$)	99.29987	1.125E-5	9.2	2.9×10^5
CH ₃ CHO($5_{1,4} - 4_{1,3}$) E	98.86331	3.104E-5	16.6	1×10^6
CH ₃ CHO($5_{1,4} - 4_{1,3}$) A	98.90095	3.108E-5	16.5	1×10^6
HC ₃ N(11 – 10)	100.07639	0.777E-4	28.8	1.5×10^6
H40 α	99.02295	-	-	-

^a Calculated assuming a gas temperature of 100 K. Critical densities are calculated as $n_{crit} = A_{ul}/\gamma_{ul}$, where A_{ul} is the Einstein coefficient and γ_{ul} is the collisional rate. The values at 100 K are taken from the Leiden Atomic and Molecular Database (Schöier et al. 2005) and the JPL spectroscopic database (Pickett et al. 1998). As no collisional rate is available for CH₃CHO($5_{1,4} - 4_{1,3}$), its critical density is estimated using the collisional rate of CH₃OH as a close approximation.

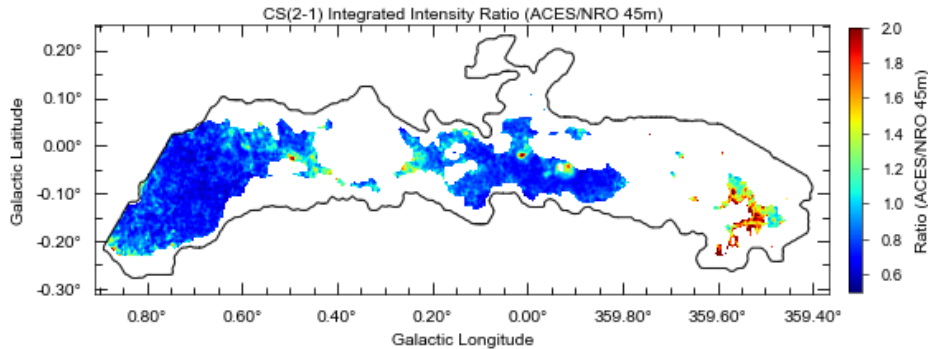


Figure 2. The ratio of ACES and NRO 45m map. The ratio map was made with the integrated intensity maps.

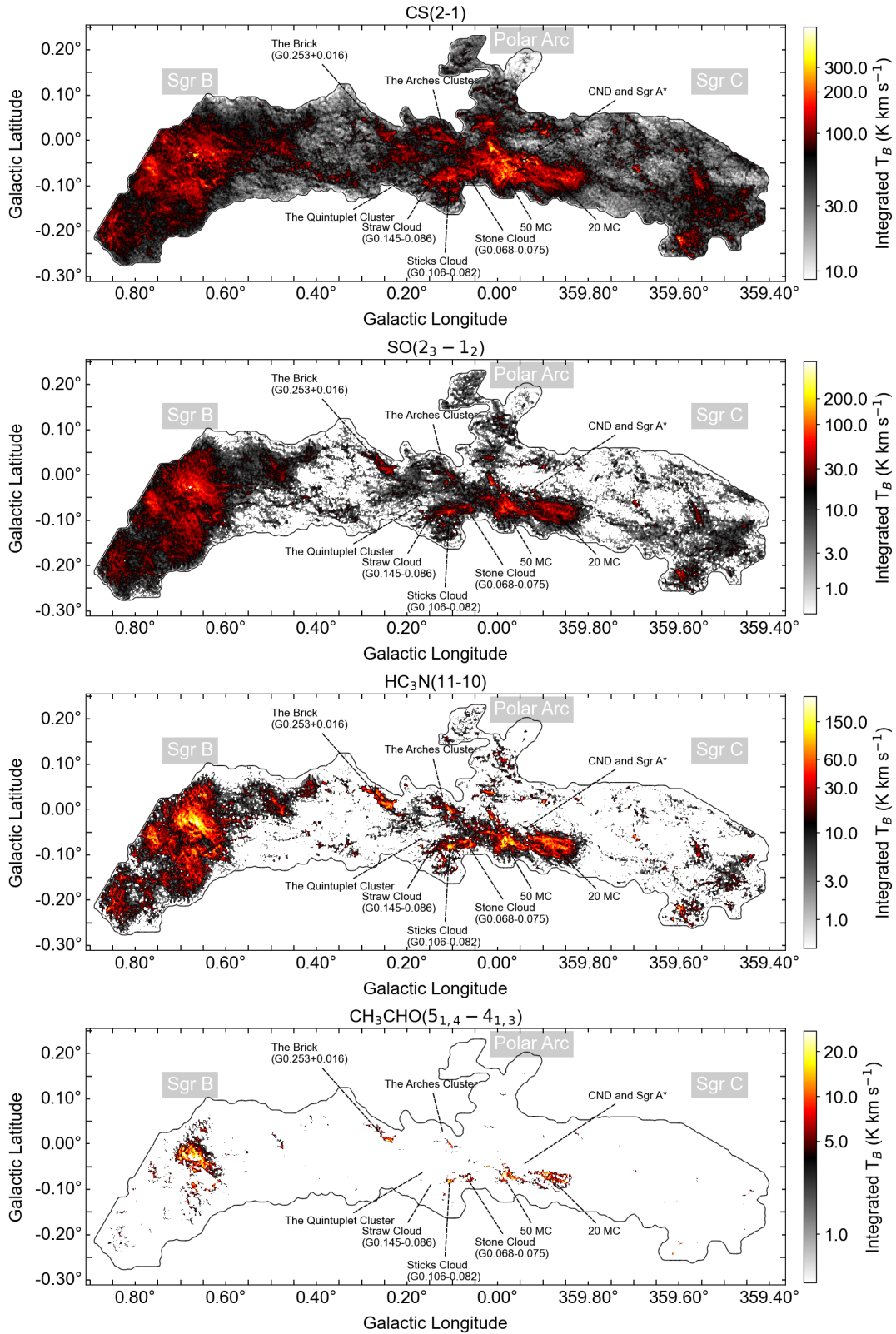


Figure 3. ALMA integrated intensity maps (mom 0) of CS(2 – 1), SO(2₃ – 1₂), HC₃N(11 – 10) and CH₃CHO(5_{1,4} – 4_{1,3}) lines towards the CMZ. The nomenclature of previously identified features are labeled. The common beam size is 2.84'' × 2.11'' with a position angle of –89.46° for the CS(2 – 1), SO(2₃ – 1₂), and CH₃CHO(5_{1,4} – 4_{1,3}) lines. The common beam size is 2.65'' × 1.97'' with a position angle of –89.96° for the HC₃N(11 – 10) line. Note that the acetaldehyde line (CH₃CHO(5_{1,4} – 4_{1,3})) maps are integrated with CH₃CHO(5_{1,4} – 4_{1,3}) E and CH₃CHO(5_{1,4} – 4_{1,3}) A.

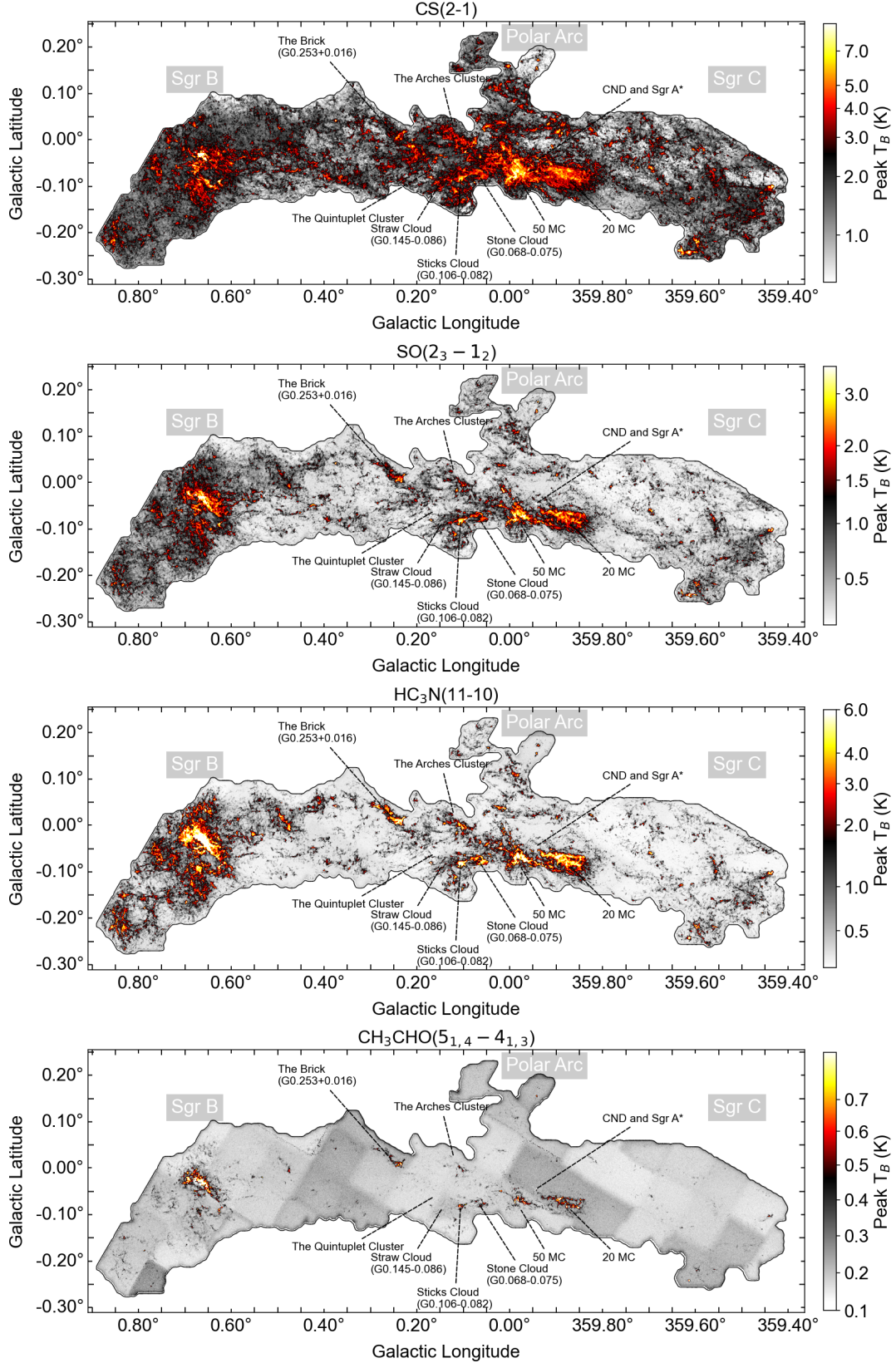


Figure 4. ALMA peak intensity maps (mom 8) of CS(2 - 1), SO(2₃ - 1₂), HC₃N(11 - 10) and CH₃CHO(5_{1,4} - 4_{1,3}) lines towards the CMZ. Note that the acetaldehyde line (CH₃CHO(5_{1,4} - 4_{1,3})) maps are stacked with CH₃CHO(5_{1,4} - 4_{1,3}) E and CH₃CHO(5_{1,4} - 4_{1,3}) A (also see Figure 1).

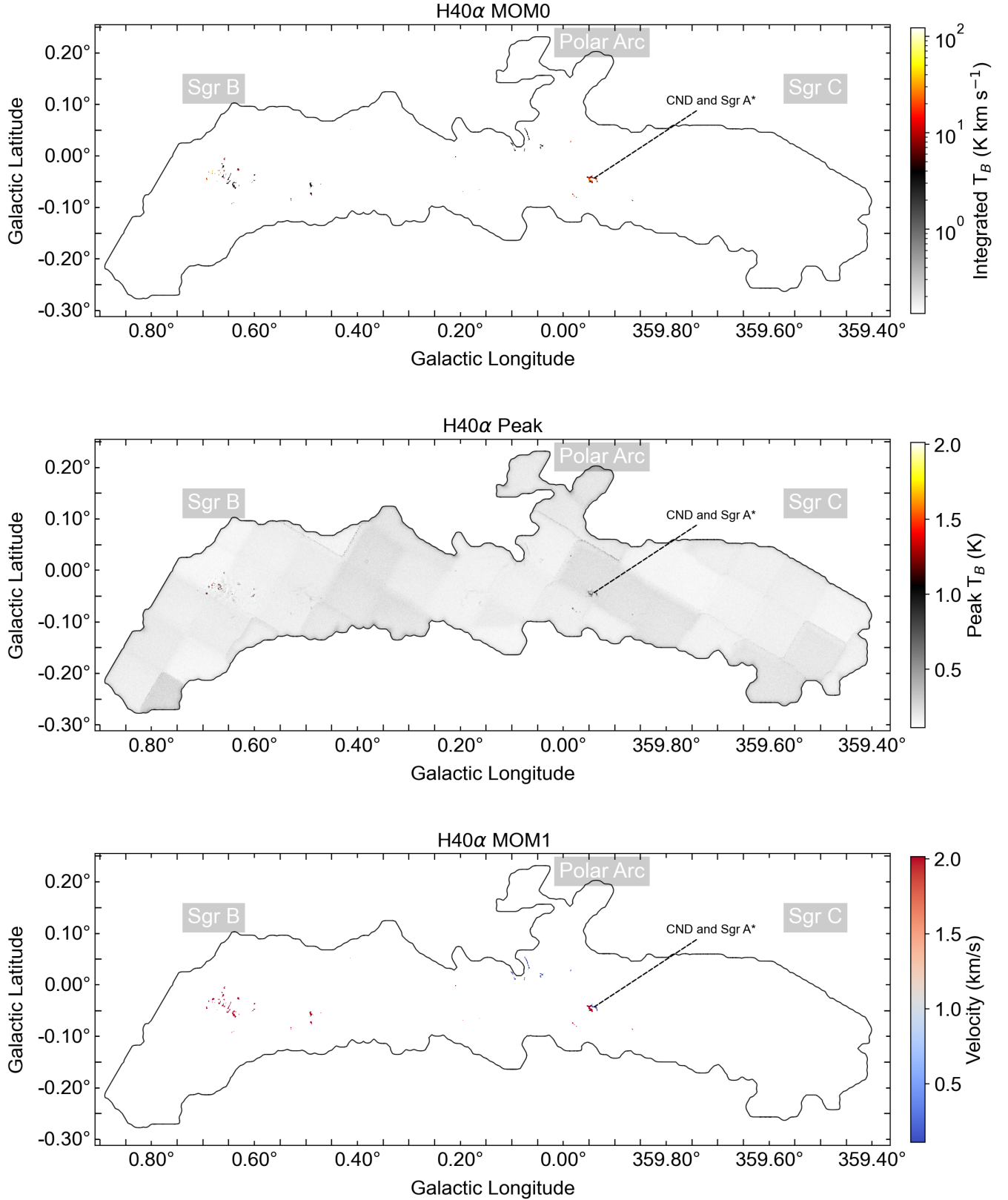


Figure 5. ALMA mosaic map of H40 α line towards the CMZ. From the top to the bottom we present the mom 0, peak intensity, and mom 1 images. The common beam size is $2.84'' \times 2.11''$ with a position angle of -89.46° .

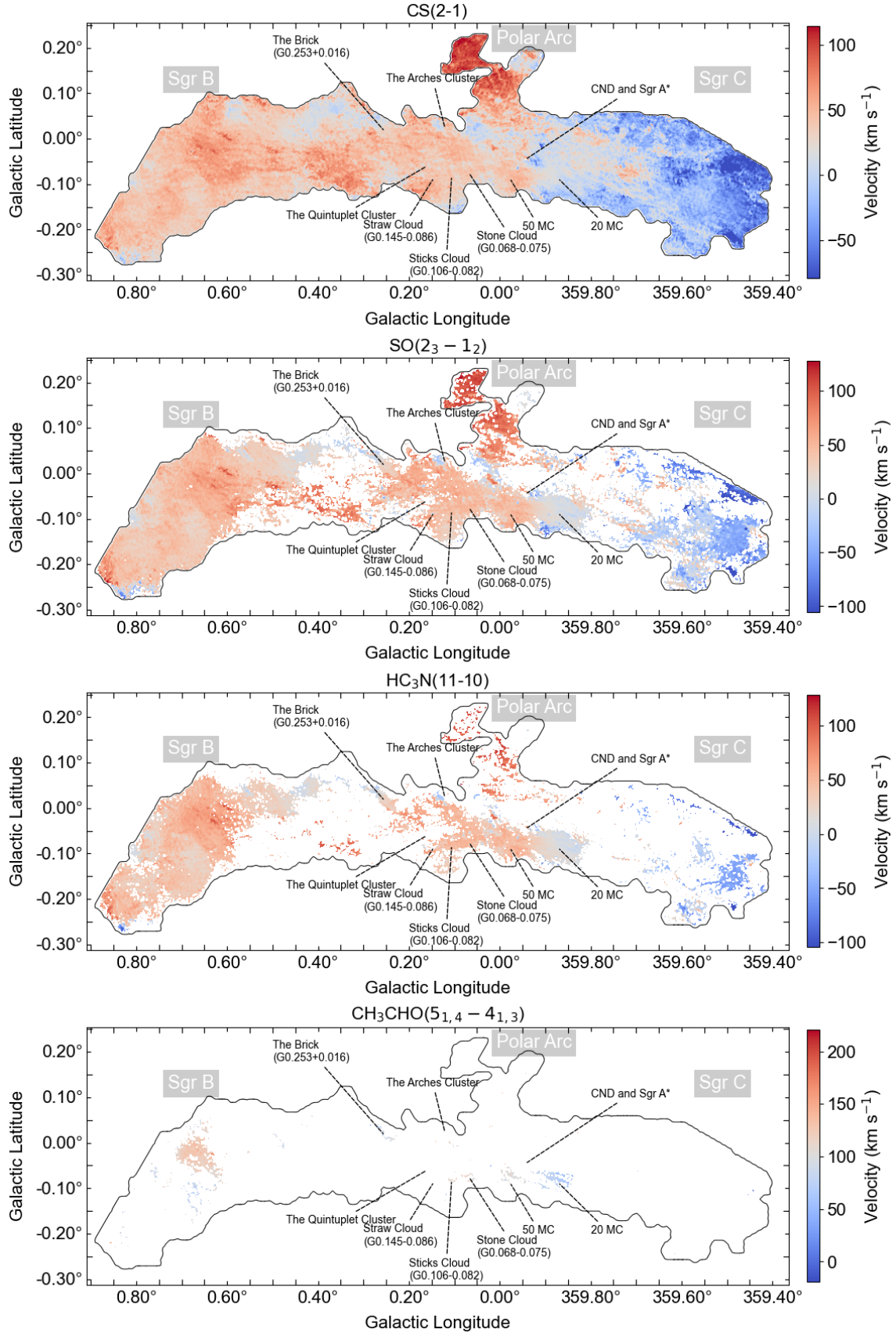


Figure 6. The intensity weighted velocity map (mom 1) of CS(2 - 1), SO(2₃ - 1₂), HC₃N(11 - 10) and CH₃CHO(5_{1,4} - 4_{1,3}) lines towards the CMZ.

The moment maps provide a detailed view of the spatial distribution of emission across the CMZ. In general the ALMA maps show a combination of extended emission and compact features. The $\text{SO}(2_3-1_2)$ and $\text{CS}(2-1)$ maps reveal a smooth and diffuse emission structure, highlighting extended regions of molecular gas across the CMZ. In contrast, the $\text{CH}_3\text{CHO}(5_{1,4}-4_{1,3})$ map is more concentrated towards the Brick, the 20 km s^{-1} cloud, the 50 km s^{-1} cloud, and the Sgr B region. The $\text{HC}_3\text{N}(11-10)$ emission exhibits an intermediate morphology, sharing characteristics of both the extended $\text{SO}(2_3-1_2)$ and $\text{CS}(2-1)$ emission and the compact $\text{CH}_3\text{CHO}(5_{1,4}-4_{1,3})$ structures. The $\text{H}40\alpha$ map displays distinct, compact emission structures that are characteristic of ionized gas. A zoomed-in view of the $\text{H}40\alpha$ map with significant detection is shown in Figure A1. Together, these maps provide a multi-line view of the gas properties, distinguishing between ionized and molecular components, and reveal the physical and chemical conditions of the observed region. However, since the molecular lines ($\text{CS}(2-1)$, $\text{CH}_3\text{CHO}(5_{1,4}-4_{1,3})$, $\text{SO}(2_3-1_2)$, and $\text{HC}_3\text{N}(11-10)$) primarily trace molecular gas that is spatially anti-correlated with the ionized gas traced by $\text{H}40\alpha$ (cf. Figure B1), a comparison between the $\text{H}40\alpha$ emission and the continuum is more physically relevant. Therefore, we do not discuss the $\text{H}40\alpha$ properties in detail in this paper. Readers are referred to Ginsburg & ACES Team (2025) for a detailed description of the continuum emission. Although that work does not discuss the $\text{H}40\alpha$ line, a direct comparison with the maps presented here may help to examine the spatial relation between ionized and molecular components.

The characteristic kinetic temperature in the CMZ has been reported as $65 \pm 10 \text{ K}$ by Ao et al. (2013) and within the range of $50-100 \text{ K}$ (Ginsburg et al. 2016; Krieger et al. 2017). As shown in Figure 4, $\text{CS}(2-1)$ exhibits a peak brightness temperature of approximately 10 K , particularly toward the Sgr A and Sgr B regions. This relatively high brightness temperature, comparable to the typical kinetic temperature in the CMZ, suggests that $\text{CS}(2-1)$ emission is generally optically thick or moderately thick, tracing gas with significant optical depth across most regions.

In contrast, $\text{SO}(2_3-1_2)$ and $\text{HC}_3\text{N}(11-10)$ show peak brightness temperatures of about $4-6 \text{ K}$. Although lower than that of $\text{CS}(2-1)$, these values indicate that the lines are moderately optically thin to moderately thick, likely reflecting somewhat lower column densities or smaller beam filling factors compared to $\text{CS}(2-1)$.

Meanwhile, $\text{CH}_3\text{CHO}(5_{1,4}-4_{1,3})$ shows a peak brightness temperature of $\leq 1 \text{ K}$, indicating that its emission might be optically thin across most of the mapped region, similar to the HC^{15}N line reported in Paper IV. With additional SO transitions available in the ACES data (Paper I), including the isotopologue line $^{34}\text{SO}(2_3-1_2)$, which is expected to be optically thin, as well as $\text{SO}(2_2-1_1)$ and $\text{SO}(5_4-4_4)$, future studies can derive detailed temperature and density distributions to better characterize the excitation conditions in various regions of the CMZ.

3.2 $\text{mom } 1$ map and longitude-velocity maps

In Figure 6, we present the $\text{mom } 1$ images of four molecular lines of the CMZ. The $\text{mom } 1$ map of $\text{H}40\alpha$ is shown separately in Figure 5. Despite being derived from high-resolution ALMA data, the velocity fields reveal large-scale coherent rotation, with redshifted emission at positive longitudes and blueshifted emission at negative longitudes, consistent with previous single-dish observations (e.g., Jones et al. 2012). On smaller scales, several regions show overlapping red- and blueshifted components, indicative of multiple gas streamers or distinct kinematic features along the line of sight (e.g., Henshaw et al. 2016; Lipman et al. 2025; Walker et al. 2025).

In Figure 7, we present the longitude-velocity ($l-v$) diagrams of the four molecular lines showing intensity peaks. In the $\text{CS}(2-1)$ line, the horizontal absorption features at -52 , -28 , and -3 km s^{-1} are due to foreground absorption, which is attributed to gas in spiral arms along the line of sight at these velocities (Jones et al. 2012). The same features can be seen in other abundant molecules such as HCO^+ (Paper III). However, these foreground absorption features are not found in the other lines presented in this paper.

These complex motions associated with sub-pc scale filaments and broad-linewidth clumps observed in the velocity map are more clearly revealed in the $l-v$ diagrams. Towards the Sgr A complex region, in Figure 8, we present the $l-v$ diagram of the CND . The streamers are shown as in the previous work by Hsieh et al. (2017). The high-velocity gas standing out from the CMZ ring (associated with the 50 and 20 km s^{-1} clouds in this figure) represents the CND and the streamers, which are kinematically distinct in both velocity structure and spatial location. These features also exhibit significantly broader linewidths ($\geq 30 \text{ km s}^{-1}$) compared to the surrounding CMZ gas, further highlighting their dynamic nature associated with tidal disruption in the deep potential well. The high spectral and spatial resolution mosaic map will enable study the infall of gas further out.

In comparison to the $l-v$ diagrams in Jones et al. (2012) at $39''$ resolution, while the Mopra data successfully traces the large-scale spiral arm structure and provides a comprehensive view of the galactic-scale kinematics across the CMZ at sub-pc scale. The low spatial resolution limits the study of motion of gas connected the CMZ and the CND . The broad linewidths clumps present in several places of the CMZ are also marginally resolved in the Mopra data. The broad linewidth clumps characteristic of the turbulent and shocked gas in this environment, leaving the physical origin and role of these velocity components unclear. ALMA data represent a crucial intermediate scale that bridges the gap between the large-scale dynamics captured by single-dish surveys and the sub-pc clumps, showing the necessity of high angular resolution observations to fully characterize the complex interplay between inflow, turbulence, and star formation in Galactic center environments.

3.3 Key Structures

In Figures 8, 9, 10, 11, and 12, we show zoomed-in images of the four molecular lines toward the well-known features interesting for star formation in the CMZ, namely, the CND , the Brick cloud, the 20 and 50 km s^{-1} clouds, and the Three Little Pigs (Sticks, Straw, and Stone clouds).

3.3.1 The circumnuclear disk

The circumnuclear disk (CND) is a molecular ring rotating around Sgr A*. It contains a molecular gas mass of approximately $10^4 M_\odot$ (e.g. Requena-Torres et al. 2012; Mills et al. 2013; Hsieh et al. 2021) and with a radius of $\sim 2 \text{ pc}$. Within this region lie the ionized streamers known as the mini-spiral (or Sgr A West; Zhao et al. 2009) (Figure A1 in this paper) and the nuclear star cluster (Figer et al. 1999). The streamers surrounding the CND are thought to be tidally stretched gas originating from nearby clouds (the 50 and 20 km s^{-1} clouds) that is accreting onto the CND . As the most massive and closest molecular reservoir to Sgr A*, the CND is of great interest for understanding both the fueling of the central black hole and nuclear star formation. The ACES high-resolution mosaic of the nuclear region enables studies of gas inflow kinematics and chemical conditions from the CMZ to the CND (e.g. Sofue et al. 2025).

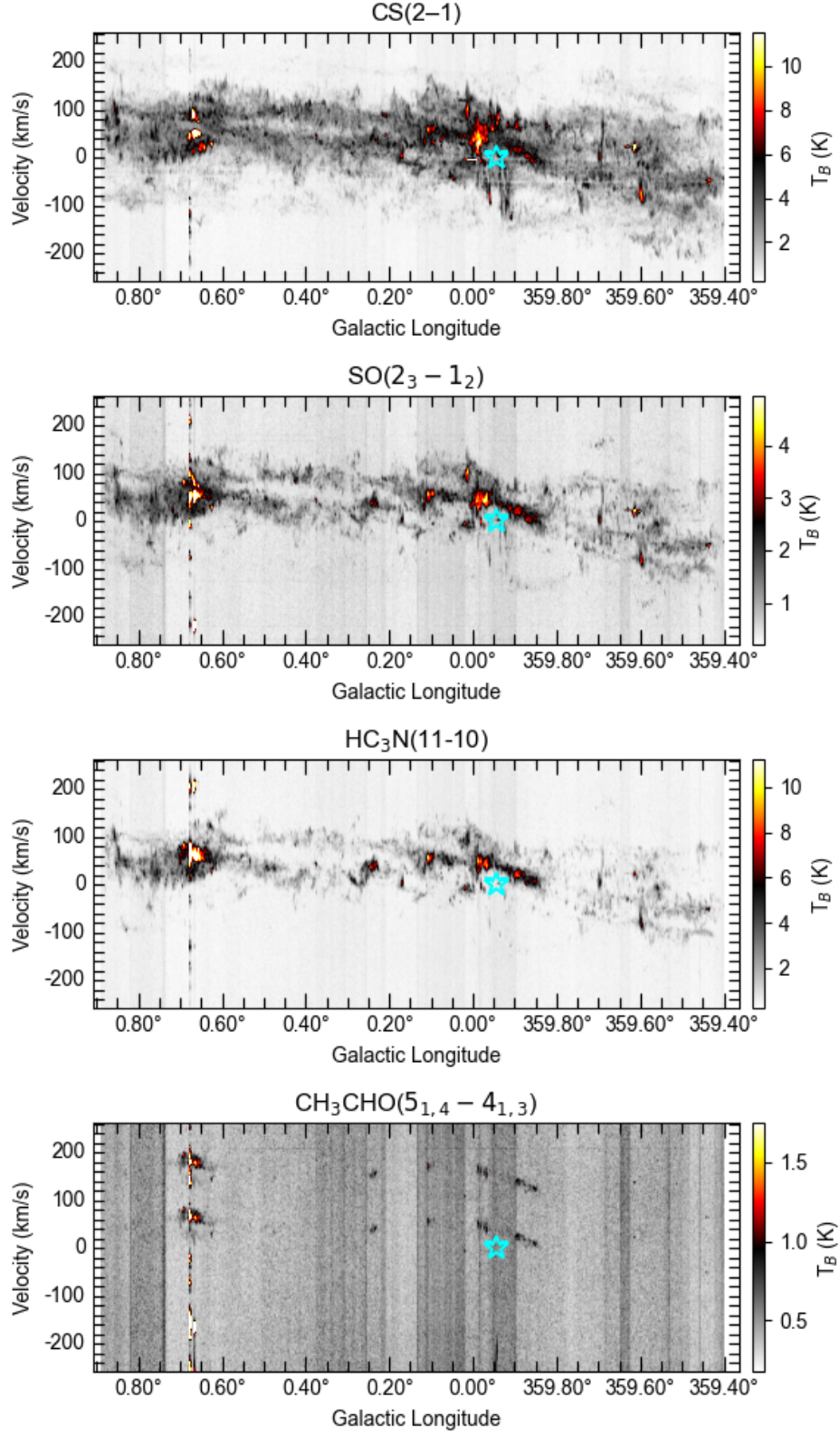


Figure 7. The Longitude-velocity diagram of CS($2 - 1$), SO($2_3 - 1_2$), HC₃N($11 - 10$) and CH₃CHO($5_{1,4} - 4_{1,3}$) lines towards the CMZ. The location of Sgr A* is labeled with the cyan star. The CH₃CHO($5_{1,4} - 4_{1,3}$) E ($f_{\text{rest}} = 98.86331$ GHz), and CH₃CHO($5_{1,4} - 4_{1,3}$) A ($f_{\text{rest}} = 98.9005$ GHz) can be seen together in the diagram, where we set the rest frequency of CH₃CHO($5_{1,4} - 4_{1,3}$) A.

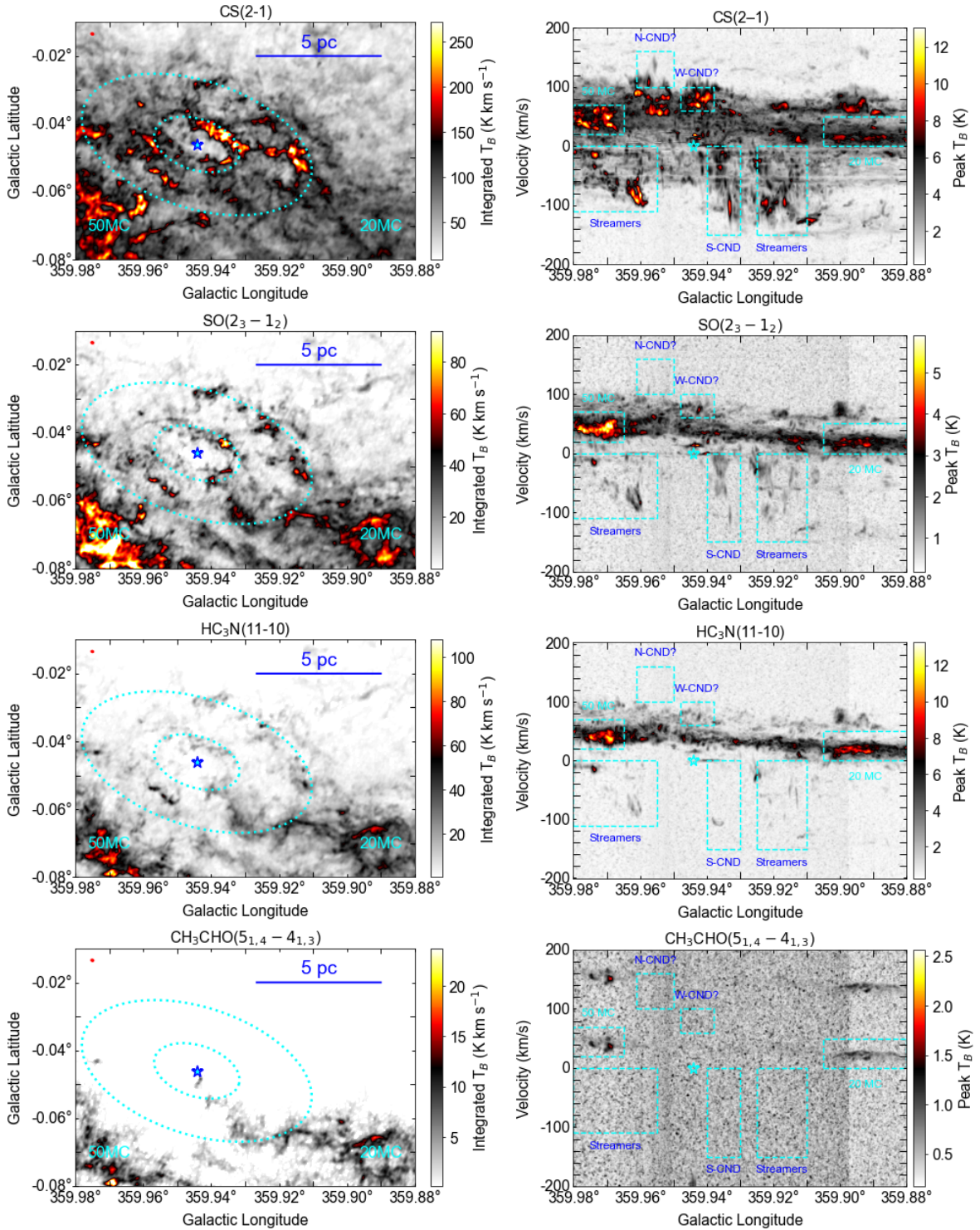


Figure 8. Left: the m_0 image of the CND. Sgr A* is marked with a cyan star, and the CND is outlined with a small cyan dotted ellipse. The streamers are outlined with the big ellipse (Liu et al. 2013; Hsieh et al. 2017). The CS(2-1), SO(2₃-1₂), HC₃N(11-10) and CH₃CHO(5_{1,4}-4_{1,3}) line images are presented. The beam is shown in the top left corner as a red filled ellipse. Right: the longitude-velocity diagrams of the four molecular lines zoomed-in to the region of the CND.

In Figure 8, the CND and the streamers (Liu et al. 2013; Hsieh et al. 2017, 2021) are outlined with small and large cyan dotted ellipses, respectively. Both the CND and the streamers are detected in the CS(2-1), SO(2₃-1₂), and faint emission with HC₃N(11-10)

lines; however, only the streamers visually connecting to the 20 km s⁻¹ cloud are detected in the CH₃CHO(5_{1,4}-4_{1,3}) line.

In the vicinity of the nuclear star cluster and Sgr A*, UV fields can photodissociate and deplete HC₃N, although the molecule may still survive in dense, well-shielded clumps (Rodriguez-Franco et al.

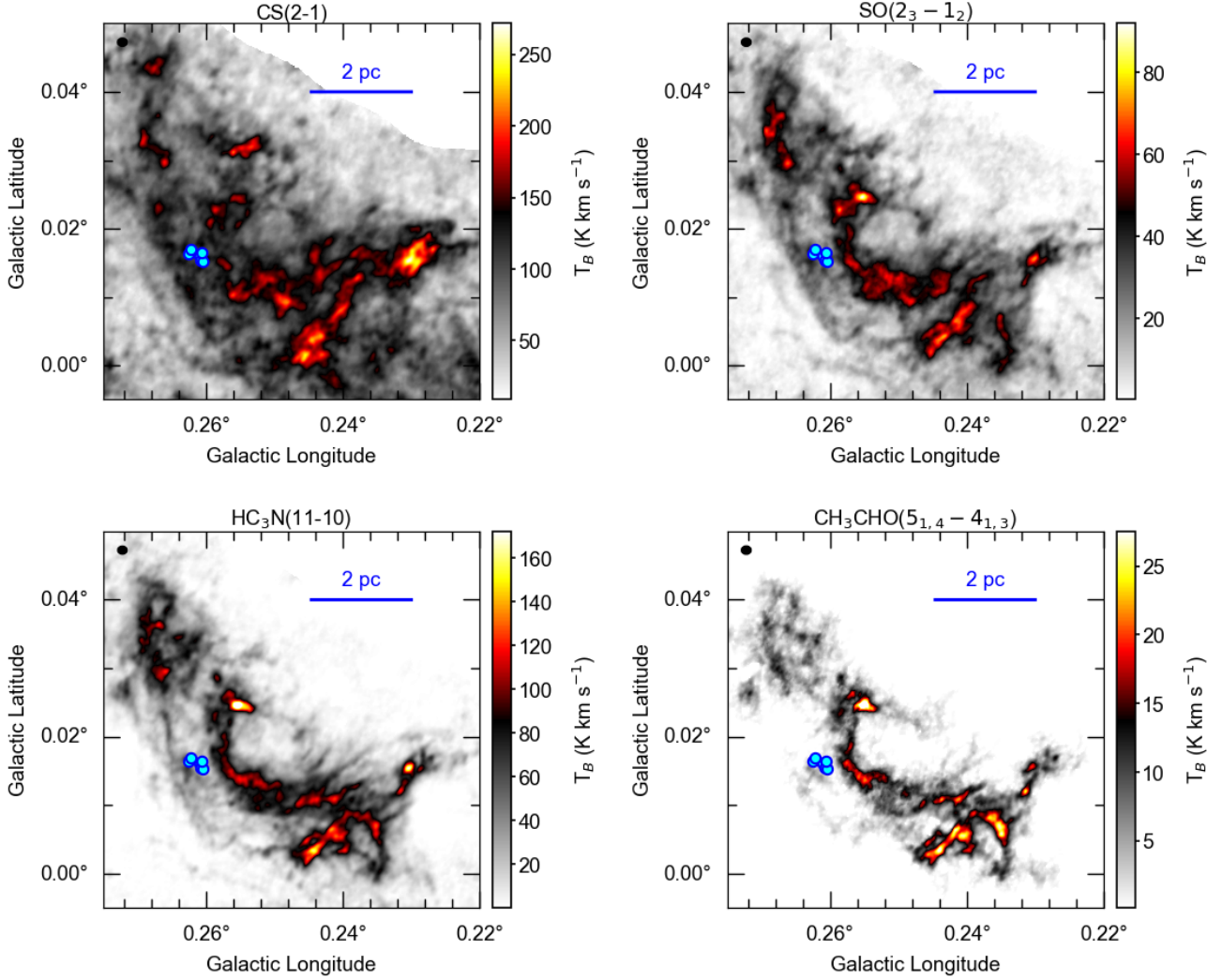


Figure 9. The $\text{mom } 0$ images of the Brick cloud (G0.253+0.016). The CS(2 – 1), SO(2₃ – 1₂), HC₃N(11 – 10) and CH₃CHO(5_{1,4} – 4_{1,3}) line images are presented. The outflow positions featuring ongoing star formation are labeled with the cyan circles (Walker et al. 2021). The synthesized beam is shown on the top left corner with a red ellipse.

1998; Meier & Turner 2005; Martín et al. 2012; Harada et al. 2015; Lindberg et al. 2011). The weak HC₃N(11 – 10) emission in the ACES map could therefore arise from a combination of UV photodissociation and excitation effects, as the warm gas in the CND may preferentially populate higher- J transitions. To quantify the relative effect of UV shielding and excitation, future observations of high-excitation HC₃N lines and detailed abundance analyses will be required, which we leave for community follow-up.

3.3.2 The Brick

G0.253+0.016, an infrared dark cloud known as “the Brick”, is one of the most massive and dense molecular clouds in the CMZ. It has a low dust temperature of 20 K, a n_{H_2} of $\geq 10^4 \text{ cm}^{-3}$, and a large gas mass of $\geq 10^5 M_{\odot}$ within size of 2–3 pc. It is considered an ideal site for forming high-mass stars (Lis & Carlstrom 1994; Lis et al. 2001). Despite having the right conditions for star formation, it shows little to no star formation activity (e.g. Immer et al. 2012;

Kauffmann et al. 2013; Rathborne et al. 2014). Although the Brick does not yet harbor fully formed massive stars or clusters, previous ALMA observations have shown evidence of ongoing intermediate-to-high-mass star formation, including the detection of seven outflow features (Walker et al. 2021).

CH₃CHO(5_{1,4} – 4_{1,3}) and SO(2₃ – 1₂) were previously imaged towards the Brick cloud by Rathborne et al. (2015) with ALMA. Although the sensitivity and resolution are slightly higher in their data, we have imaged additional CS(2 – 1) and HC₃N(11 – 10) lines with a larger mosaic. In Figure 9, the Brick cloud exhibits arm-like internal structures (Johnston et al. 2014), and CH₃CHO(5_{1,4} – 4_{1,3}) emission is relatively brighter in the southern part of the cloud. While both CS(2 – 1) and SO(2₃ – 1₂) exhibit widespread emission tracing the filaments and seem to be immersed in the diffuse arm-like structures in the CMZ, the emission from CH₃CHO(5_{1,4} – 4_{1,3}) line is much more compact and spatially confined.

The CH₃CHO(5_{1,4} – 4_{1,3}) emission appears to be well separated from the diffuse large-scale arms and instead traces distinct

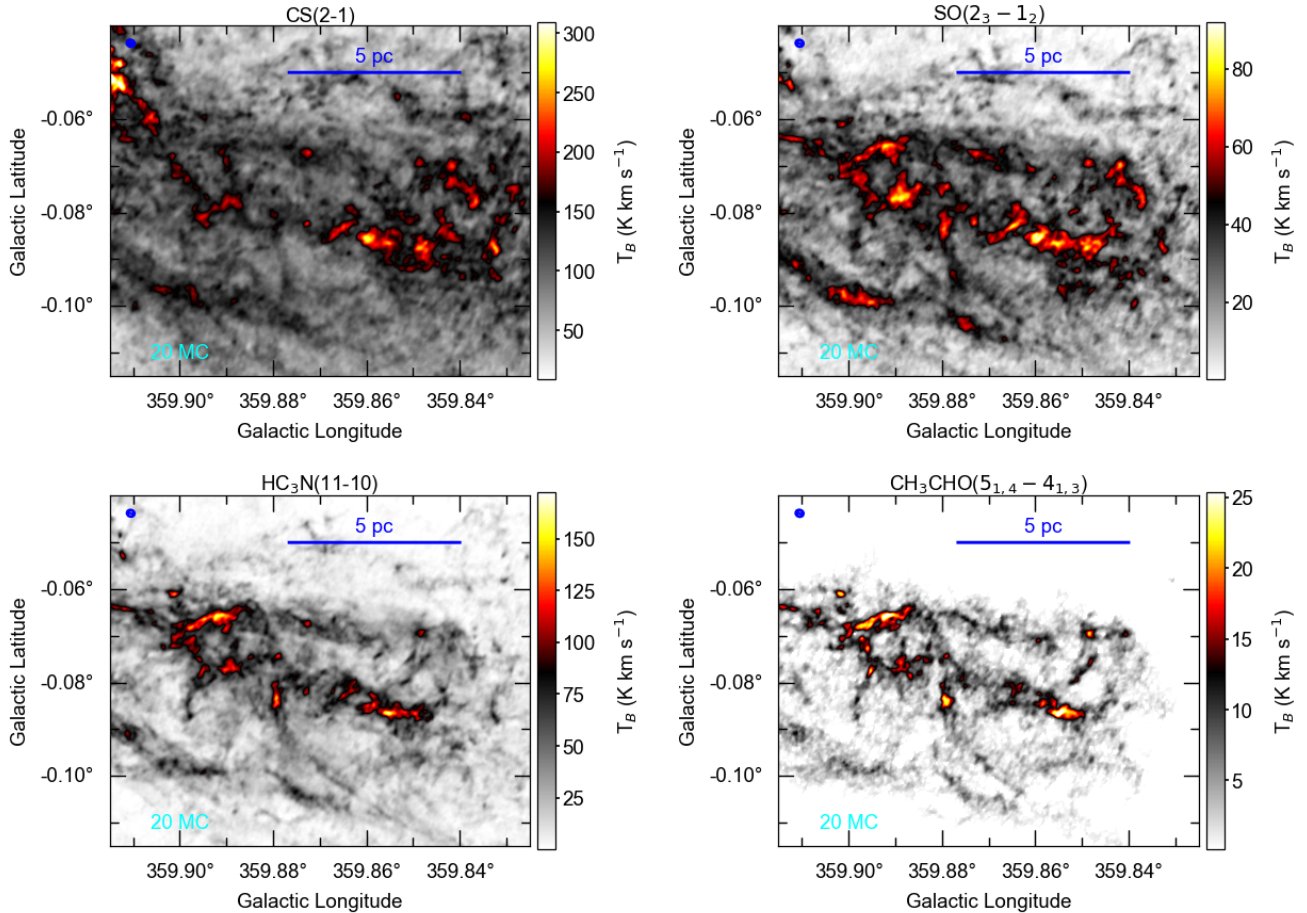


Figure 10. The $\text{mom } 0$ images of the 20 km s^{-1} cloud. The CS(2 – 1), SO($2_3 - 1_2$), HC₃N(11 – 10) and CH₃CHO($5_{1,4} - 4_{1,3}$) line images are presented. The synthesized beam is shown on the top left corner with a blue ellipse.

clumps concentrated within the central ridges of the Brick. The CH₃CHO($5_{1,4} - 4_{1,3}$) line exhibits morphologies similar to those of HC₃N(11 – 10), tracing a coherent network of compact clumps and ridges. These features are especially prominent along the southern ridge and central arc. This visual similarity is quantified by a high 2D morphological correlation coefficient of 0.9 (Figure B1, more description in Paper IV). The SO($2_3 - 1_2$) line also shows significant overlap with HC₃N(11 – 10), capturing many of the same structures, though with slightly more diffuse emission. The SO($2_3 - 1_2$)–HC₃N(11 – 10) correlation is also high, at 0.94, indicating strong morphological similarity. In contrast, the CS(2 – 1) emission displays a more extended and diffuse distribution, particularly toward the northern regions. It shows weaker overlap with both CH₃CHO($5_{1,4} - 4_{1,3}$) (correlation coefficient=0.35) and HC₃N(11 – 10) (correlation coefficient=0.66), but aligns relatively well with SO($2_3 - 1_2$) (correlation coefficient=0.8). The variation in internal structures among the four lines suggests that the compact features within the Brick vary chemically and physically.

3.3.3 The 20 and 50 km s^{-1} cloud

The 20 km s^{-1} cloud and the 50 km s^{-1} cloud are prominent giant molecular clouds in the CMZ (e.g., Uehara et al. 2019; Lu et al. 2021), specifically, near the Sgr A*.

The 20 km s^{-1} cloud shows signs of early-stage star formation, including the detection of protostellar outflows in the SiO($5-4$) line (Lu et al. 2021). In contrast, the 50 km s^{-1} cloud does not exhibit clear protostellar outflow signatures and currently has low star formation rate ($\leq 0.3 \times 10^{-3} M_{\odot}$, Lu et al. 2021), but it is likely in a later stage of star formation (Mills et al. 2011), as it lies adjacent to the compact H II region complex G–0.02 – 0.07 (Figure A1 in this paper) (Tsuboi et al. 2019; Mills et al. 2011), which shares a similar velocity structure. While the 50 km s^{-1} cloud is currently inactive in star formation, Miyawaki et al. (2021) reported the detection of 28 hot molecular core candidates, which are in quasi-static equilibrium.

Figures 10 and 11 show the detection of CH₃CHO($5_{1,4} - 4_{1,3}$) emission toward the 20 and 50 km s^{-1} clouds, respectively. As in the Brick cloud, CH₃CHO shows a high correlation with HC₃N (0.9), a moderate correlation with SO (0.69), and a low correlation with CS (0.34).

3.3.4 The three little pigs (TLP)

The Three Little Pigs (TLP) cloud complex consists of four molecular clouds known as the Straw (M0.145-0.086), the Sticks (M0.106-0.082), and the Stone (M0.068-0.075) (Battersby et al. 2020) from the left to the right side in Figure 12. Consistent with the previous SMA 1 mm image (Battersby et al. 2020), the morphology of the

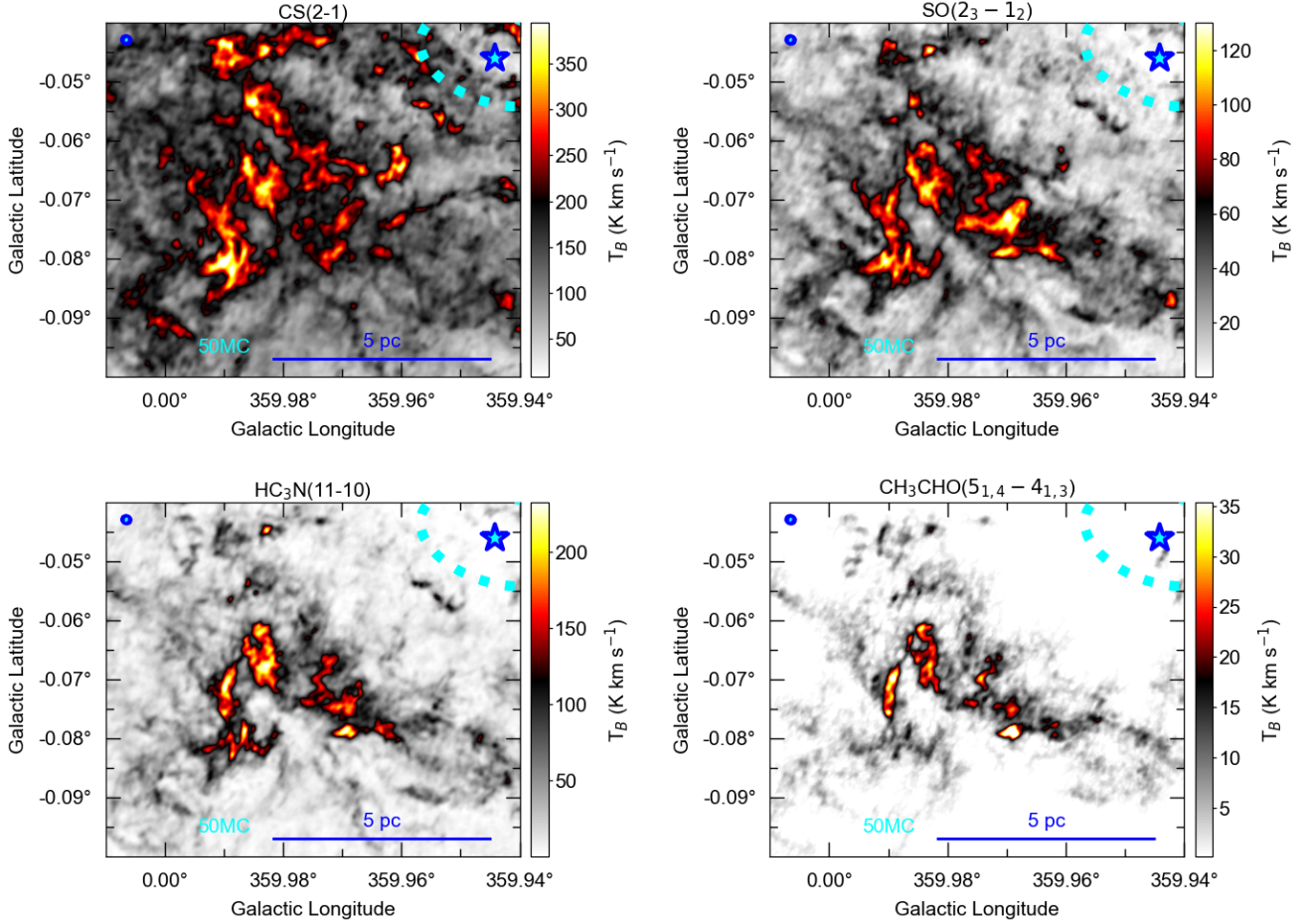


Figure 11. The $m\sigma$ images of the 50 km s^{-1} cloud. The Sgr A* is labeled with the blue star. The CNB is outlined with a cyan dotted line. The CS(2 – 1), SO($2_3 - 1_2$), HC₃N(11 – 10) and CH₃CHO($5_{1,4} - 4_{1,3}$) line images are presented. The synthesized beam is shown on the top left corner with a blue ellipse.

TLP clouds appears to become progressively more complex from the straw cloud to the stone cloud. The straw cloud is very faint in lines, possibly quiescent or less evolved. The sticks cloud appears to be the most prominent in these four molecular lines, showing compact clumps in all three tracers. Similar to the aforementioned clouds, we find a consistent trend in the morphological correlations among these four lines: CH₃CHO shows the highest correlation with HC₃N (0.89), an intermediate correlation with SO (0.77), and the lowest correlation with CS (0.59).

4 MORPHOLOGICAL CORRELATIONS BETWEEN THE CS(2 – 1), SO($2_3 - 1_2$), HC₃N(11 – 10), CH₃CHO($5_{1,4} - 4_{1,3}$) AND SIO(2-1)

In Figure B1, we find that CH₃CHO($5_{1,4} - 4_{1,3}$) shows the highest correlation with HC₃N(11 – 10) (0.84–0.9 across the four highlighted regions), an intermediate correlation with SO($2_3 - 1_2$) (0.64–0.69), and the weakest correlation with CS(2 – 1) (0.25–0.59). This consistent pattern across all regions suggests that CH₃CHO($5_{1,4} - 4_{1,3}$) emission is more spatially similar to HC₃N(11 – 10) than with CS(2 – 1). Although the CS molecule is widely used dense-gas tracer because of the large dipole moment and high critical densities, its high abundance often leads to significant optical depth, limiting its reliability

for tracing the most compact, high-column structures. Pety et al. (2017) showed that CS emission mainly traces gas at intermediate column densities and saturates in the densest regions, while CS(1–0) in the CMZ shows moderate optical depths of $\tau \lesssim 2-3$ (Tsuboi et al. 1999), consistent with its widespread distribution across the CMZ clouds.

The critical densities of CS(2 – 1) and SO($2_3 - 1_2$) are roughly an order of magnitude lower than those of CH₃CHO($5_{1,4} - 4_{1,3}$) and HC₃N(11 – 10). Although we have not directly derived the gas densities here, at first glance, the correlation coefficients suggest that CS(2 – 1) and SO($2_3 - 1_2$) trace more extended dense gas, whereas CH₃CHO($5_{1,4} - 4_{1,3}$) and HC₃N(11 – 10) highlight more compact, denser substructures. However, CH₃CHO($5_{1,4} - 4_{1,3}$) emission does not necessarily trace dense cores exclusively (Ikeda et al. 2001; Jørgensen et al. 2016; Codella et al. 2017; Oya et al. 2017); given its relatively low abundance and the subthermal excitation of its low- J transitions at moderate densities ($\sim 10^{4-5} \text{ cm}^{-3}$), its detection may be biased toward high-column-density regions that exceed the sensitivity threshold rather than reflecting a true absence elsewhere (e.g., Requena-Torres et al. 2006; Jimenez-Serra et al. 2025). Observations of optically thin isotopologues such as HC¹⁵N (Paper III) could therefore help disentangle optical-depth effects and confirm the effectiveness of these molecules as dense-gas tracers.

In Figure B1, SO($2_3 - 1_2$), HC₃N(11 – 10), and CH₃CHO($5_{1,4} -$

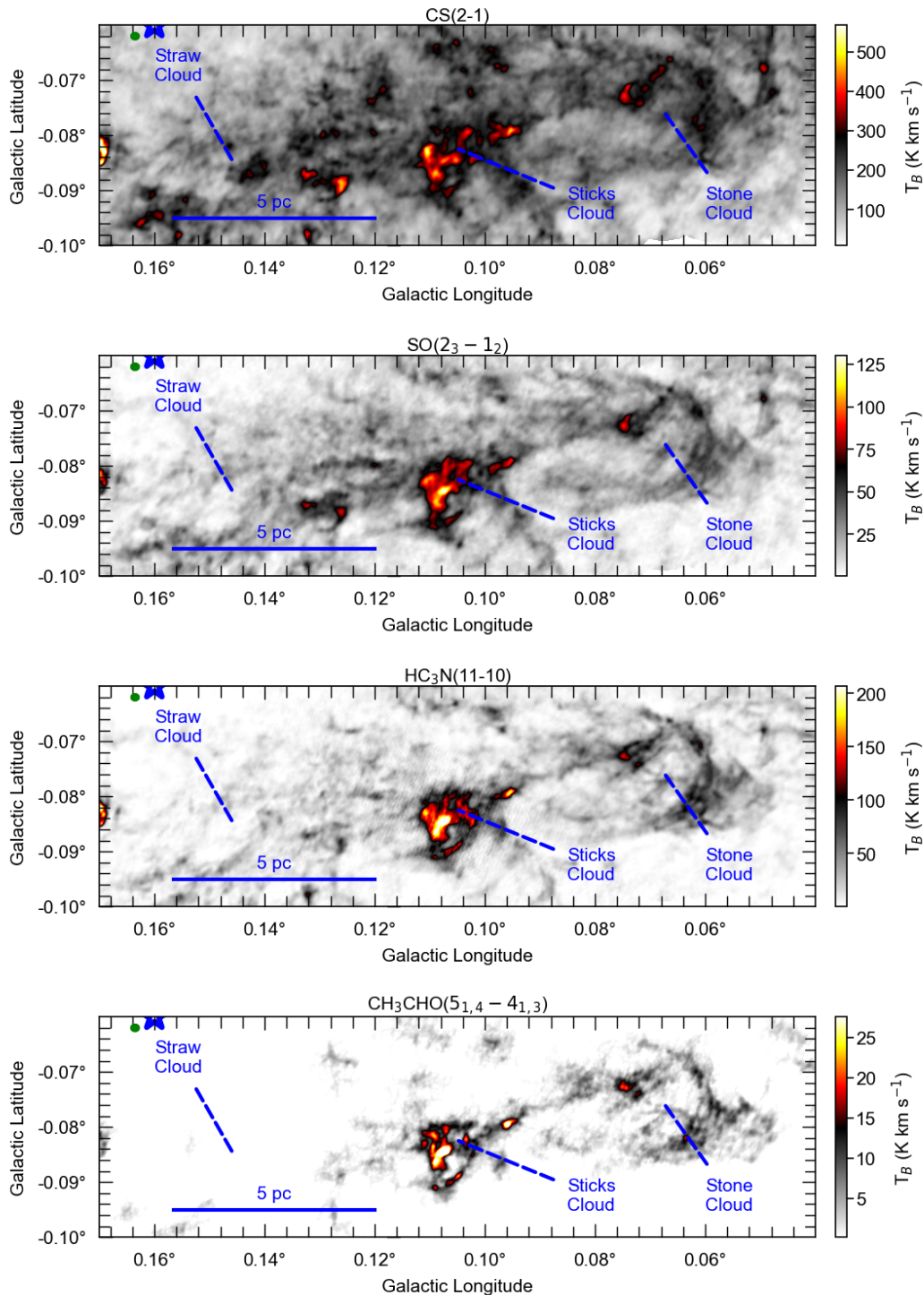


Figure 12. The m_0 images of the three little pigs cloud (stone, sticks, and straw cloud). The CS(2–1), SO(2_3-1_2), HC₃N(11–10) and CH₃CHO($5_{1,4}-4_{1,3}$) line images are presented. The synthesized beam is shown on the top left corner with a blue ellipse.

$4_{1,3}$) show stronger correlations with SiO than with CS across the four regions and in the CMZ average (Paper III). SiO is a well-established shock tracer (Schilke et al. 1997), and its widespread CMZ emission likely reflects large-scale shocks driven by, for example, expanding H_{II} regions or supernova remnants (Inutsuka 2021; Henshaw et al. 2022), cloud–cloud collisions (Tsuboi et al. 2015; Zeng et al. 2020),

or Galactic shear (Kruijssen et al. 2014; Petkova et al. 2021). Additional processes such as cosmic-ray heating (Yusef-Zadeh et al. 2013) and X-ray irradiation (Martín-Pintado et al. 2000) may also influence Si-bearing chemistry.

Sulphur-bearing species such as SO can be enhanced in shock and post-shock gas (Pineau des Forets et al. 1993; Lis et al. 2001; Lu

et al. 2017; Callanan et al. 2023), although SO is not unique to shocks and also appears in relatively quiescent gas in both low- and high-mass star-forming regions (e.g. Hacar et al. 2013). $\text{HC}_3\text{N}(11-10)$ is a well-known tracer of dense, early-phase cores, forming mainly through reactions involving CN and C_2H_2 radicals (e.g. Walmsley et al. 1980; Suzuki et al. 1992), but its abundance can also increase in low-velocity shocks associated with stellar outflows (e.g., Bachiller & Pérez Gutiérrez 1997; Mendoza et al. 2018; Hoque et al. 2025). $\text{CH}_3\text{CHO}(5_{1,4}-4_{1,3})$ is typically linked to hot cores and outflows in the Galactic disk (Ikeda et al. 2001; Jørgensen et al. 2016; Codella et al. 2017; Oya et al. 2017), yet in the CMZ, COMs including $\text{CH}_3\text{CHO}(5_{1,4}-4_{1,3})$ are widespread and associated with low-velocity shocks largely independent of local star formation activity (Requena-Torres et al. 2006; Jimenez-Serra 2025; Li et al. 2025).

Across these species, the correlation strengths with SiO — SO — SiO ($0.90 > \text{HC}_3\text{N}$ — SiO (0.83) $> \text{CS}$ — SiO (0.79) $> \text{CH}_3\text{CHO}$ — SiO (0.67)) suggest different physical and chemical conditions. A detailed determination of SiO abundances and dedicated chemical modeling, along with further examination of the associations among $\text{SO}(2_3-1_2)$, $\text{HC}_3\text{N}(11-10)$, and $\text{CH}_3\text{CHO}(5_{1,4}-4_{1,3})$, will be essential to better understand the extreme environment of the CMZ. These analyses are beyond the scope of this paper and the in-depth studies are left for future studies.

5 SUMMARY

In this paper, we present an overview of the ACES broadband spectral-line data and the public release of the $\text{CS}(2-1)$, $\text{SO}(2_3-1_2)$, $\text{CH}_3\text{CHO}(5_{1,4}-4_{1,3})$, $\text{H}4\alpha$, and $\text{HC}_3\text{N}(11-10)$ mosaic images. We provide the corresponding moment maps, longitude–velocity (l - v) diagrams, and a morphological correlation analysis comparing 14 lines with the 3 mm continuum (Paper II; Paper III; Paper IV). The emissions from these molecules are widely distributed across the CMZ. The $\text{CS}(2-1)$ and $\text{SO}(2_3-1_2)$ lines exhibit more extended spatial distributions, whereas $\text{HC}_3\text{N}(11-10)$ and $\text{CH}_3\text{CHO}(5_{1,4}-4_{1,3})$ are more concentrated toward the denser regions. Comparisons with other lines, such as SO transitions and isotopologues (Paper I) will also be useful for constraining the temperature and density.

The morphological correlation analysis reveals systematic differences in how molecular species trace the physical and chemical structures within the CMZ. The stronger correlations of $\text{SO}(2_3-1_2)$, $\text{HC}_3\text{N}(11-10)$, and $\text{CH}_3\text{CHO}(5_{1,4}-4_{1,3})$ with SiO indicate that these species are more closely linked to shocked gas. These results highlight the potential of the CMZ as a laboratory for studying the properties and history of large-scale shocks and their impact on molecular chemistry. Although we have not determined SiO or other shock-related abundances here, the observed correlations provide valuable constraints for future investigations at high spatial resolution. In addition to shocks, other energetic drivers such as cosmic rays, X rays, and photodissociation regions (PDRs), as indicated by the H II regions traced by $\text{H}4\alpha$, are also likely to influence the chemical and thermal state of the gas. A comprehensive study of these processes, combining chemical modeling and multi-line diagnostics, will be essential to deepen our understanding of the interplay between dynamics and chemistry in the CMZ.

ACKNOWLEDGMENTS

We thank the anonymous referee for the careful reading and constructive comments that helped improve this paper. This paper makes use of the following ALMA data: ADS/JAO.ALMA#2021.1.00172.L. ALMA is a partnership of ESO (representing its member states), NSF (USA) and NINS (Japan), together with NRC (Canada), NSTC and ASIAA (Taiwan), and KASI (Republic of Korea), in cooperation with the Republic of Chile. The Joint ALMA Observatory is operated by ESO, AUI/NRAO and NAOJ. The authors are grateful to the staff throughout the ALMA organisation, particularly those at the European ALMA Regional Centre, the Joint ALMA Observatory, and the UK ALMA Regional Centre Node, for their extensive support, which was essential to the success of this challenging Large Program.

Data analysis was in part carried out on the Multi-wavelength Data Analysis System operated by the Astronomy Data Center (ADC), National Astronomical Observatory of Japan. D.L.W gratefully acknowledges support from the UK ALMA Regional Centre (ARC) Node, which is supported by the Science and Technology Facilities Council [grant numbers ST/Y004108/1 and ST/T001488/1]. R.F. acknowledges support from the grants PID2023-146295NB-I00, and from the Severo Ochoa grant CEX2021-001131-S funded by MCIN/AEI/ 10.13039/501100011033 and by “European Union NextGenerationEU/PRTR”. I.J.-S., L.C., and V.M.R. acknowledge support from the grant PID2022-136814NB-I00 by the Spanish Ministry of Science, Innovation and Universities/State Agency of Research MICIU/AEI/10.13039/501100011033 and by ERDF, UE. I.J.-S. also acknowledges the ERC Consolidator grant OPENS (project number 101125858) funded by the European Union. V.M.R. also acknowledges the grant RYC2020-029387-I funded by MICIU/AEI/10.13039/501100011033 and by “ESF, Investing in your future”, and from the Consejo Superior de Investigaciones Científicas (CSIC) and the Centro de Astrobiología (CAB) through the project 20225AT015 (Proyectos intramurales especiales del CSIC); and from the grant CNS2023-144464 funded by MICIU/AEI/10.13039/501100011033 and by “European Union NextGenerationEU/PRTR. The authors acknowledge UFIT Research Computing for providing computational resources and support that have contributed to the research results reported in this publication. AG acknowledges support from the NSF under grants CAREER 2142300, AAG 2008101, and particularly AAG 2206511 that supports the ACES large program. M.G.S.-M. acknowledges support from the NSF under grant CAREER 2142300. M.G.S.-M. also thanks the Spanish MICINN for funding support under grant PID2023-146667NB-I00. A.S.-M. acknowledges support from the RYC2021-032892-I grant funded by MCIN/AEI/10.13039/501100011033 and by the European Union ‘Next GenerationEU’/PRTR, as well as the program Unidad de Excelencia María de Maeztu CEX2020-001058-M, and support from the PID2023-146675NB-I00 (MCI-AEI-FEDER, UE). KMD acknowledges support from the European Research Council (ERC) Advanced Grant MOPPEX 833460.vii. X.L. acknowledges support from the Strategic Priority Research Program of the Chinese Academy of Sciences (CAS) Grant No. XDB0800300, the National Key R&D Program of China (No. 2022YFA1603101), State Key Laboratory of Radio Astronomy and Technology (CAS), the National Natural Science Foundation of China (NSFC) through grant Nos. 12273090 and 12322305, the Natural Science Foundation of Shanghai (No. 23ZR1482100), and the CAS “Light of West China” Program No. xbzg-zdsys-202212. Q. Z. gratefully acknowledges the support from the National Science Foundation under Award No. AST-2206512, and the Smithsonian Institute FY2024 Scholarly

Studies Program. FHL acknowledges support from the ESO Studentship Programme, the Scatcherd European Scholarship of the University of Oxford, and the European Research Council’s starting grant ERC StG-101077573 (‘ISM-METALS’). C. F. acknowledges funding provided by the Australian Research Council (Discovery Projects DP230102280 and DP250101526), and the Australia-Germany Joint Research Cooperation Scheme (UA-DAAD). F. M. acknowledges financial support from the School of Astronomy at the Institute for Research in Fundamental Sciences-IPM. J.K. is supported by the Royal Society under grant number RF\ERE\231132, as part of project URF\R\1\211322. MCS acknowledges financial support from the European Research Council under the ERC Starting Grant ‘GalFlow’ (grant 101116226) and from Fondazione Cariplo under the grant ERC attrattività n. 2023-3014. M.C. gratefully acknowledges funding from the DFG through an Emmy Noether Research Group (grant number CH2137/1-1). COOL Research DAO (Chevance et al. 2025) is a Decentralized Autonomous Organization supporting research in astrophysics aimed at uncovering our cosmic origins. J. Wallace gratefully acknowledges funding from National Science Foundation under Award Nos. 2108938 and 2206510. E.A.C. Mills gratefully acknowledges funding from the National Science Foundation under Award Nos. 1813765, 2115428, 2206509, and CAREER 2339670. F.N.-L. gratefully acknowledges financial support from grant PID2024-162148NA-I00, funded by MCIN/AEI/10.13039/501100011033 and the European Regional Development Fund (ERDF) ‘A way of making Europe’, from the Ramón y Cajal programme (RYC2023-044924-I) funded by MCIN/AEI/10.13039/501100011033 and FSE+, and from the Severo Ochoa grant CEX2021-001131-S, funded by MCIN/AEI/10.13039/501100011033.

SOFTWARE

This paper made use of the following software packages: **CASA** (CASA Team et al. 2022) to carry out calibration and imaging of the ALMA data, **CARTA** (Comrie et al. 2021) to visualise and analyse the data, **astropy** (Astropy Collaboration et al. 2013; Price-Whelan et al. 2018; Astropy Collaboration et al. 2022) to analyse the images and make plots, **spectral-cube** (Ginsburg et al. 2019) to process the image cubes and produce the moment maps, **radio-beam** (Koch et al. 2025) to determine (1) a common beam among multiple channels in a cube, (2) to smooth the individual channel beams to this common resolution, (3) to determine the Jy-K conversion, and **APLpy** (Robitaille & Bressert 2012) and **seaborn** (Waskom 2021) to make plots.

DATA AVAILABILITY

All data products and associated documentation can be found at <https://almascience.org/alma-data/lp/aces>. To maximise usability and provide a single, comprehensive resource for users, we also provide an online, machine-readable table, which contains the full, detailed list of all data products released for the entire survey, including hyperlinks to the full files from the ALMA archive.

All code and data processing issues are available at the public GitHub repository here: https://github.com/ACES-CMZ/reduction_ACES.

The ACES data reduction was a monolithic work that was written up in 5 papers. If you use the ACES data, please cite the appropriate works, which includes Longmore & ACES Team (2025) and the data papers: continuum (Ginsburg & ACES Team 2025) and cubes

in high-resolution (this work), medium-resolution (Lu 2025), and low-resolution (Hsieh 2025) spectral windows. Note that all papers should be cited for use of any data; the continuum imaging relied on the line papers, and vice-versa.

REFERENCES

- Ao Y., et al., 2013, *A&A*, **550**, A135
 Astropy Collaboration et al., 2013, *A&A*, **558**, A33
 Astropy Collaboration et al., 2022, *ApJ*, **935**, 167
 Bachiller R., Pérez Gutiérrez M., 1997, *ApJ*, **487**, L93
 Barnes A. T., Longmore S. N., Battersby C., Bally J., Kruijssen J. M. D., Henshaw J. D., Walker D. L., 2017, *MNRAS*, **469**, 2263
 Battersby C., et al., 2020, *ApJS*, **249**, 35
 CASA Team et al., 2022, *PASP*, **134**, 114501
 Callanan D., et al., 2023, *MNRAS*, **520**, 4760
 Chevance M., Kruijssen J. M. D., Longmore S. N., 2025, *arXiv e-prints*, p. [arXiv:2501.13160](https://arxiv.org/abs/2501.13160)
 Codella C., et al., 2017, *A&A*, **605**, L3
 Comrie A., et al., 2021, CARTA: Cube Analysis and Rendering Tool for Astronomy, Astrophysics Source Code Library, record ascl:2103.031
 De Pree C. G., Wilner D. J., Goss W. M., 2011, *AJ*, **142**, 177
 Ekers R. D., van Gorkom J. H., Schwarz U. J., Goss W. M., 1983, *A&A*, **122**, 143
 Figer D. F., Kim S. S., Morris M., Serabyn E., Rich R. M., McLean I. S., 1999, *ApJ*, **525**, 750
 Genzel R., Eisenhauer F., Gillessen S., 2010, *Reviews of Modern Physics*, **82**, 3121
 Ginsburg A., ACES Team 2025, *ApJ*, **1**, 1
 Ginsburg A., et al., 2016, *A&A*, **586**, A50
 Ginsburg A., et al., 2019, radio-astro-tools/spectral-cube: Release v0.4.5, [doi:10.5281/zenodo.3558614](https://doi.org/10.5281/zenodo.3558614)
 Hacar A., Tafalla M., Kauffmann J., Kovács A., 2013, *A&A*, **554**, A55
 Harada N., et al., 2015, *A&A*, **584**, A102
 Henshaw J. D., et al., 2016, *MNRAS*, **457**, 2675
 Henshaw J. D., et al., 2022, *MNRAS*, **509**, 4758
 Henshaw J. D., Barnes A. T., Battersby C., Ginsburg A., Sormani M. C., Walker D. L., 2023, in Inutsuka S., Aikawa Y., Muto T., Tomida K., Tamura M., eds, *Astronomical Society of the Pacific Conference Series Vol. 534, Protostars and Planets VII*. p. 83 ([arXiv:2203.11223](https://arxiv.org/abs/2203.11223)), [doi:10.48550/arXiv.2203.11223](https://doi.org/10.48550/arXiv.2203.11223)
 Ho P. T. P., Jackson J. M., Barrett A. H., Armstrong J. T., 1985, *ApJ*, **288**, 575
 Hoque A., et al., 2025, *ApJ*, **987**, 197
 Hsieh P., 2025, preprint
 Hsieh P.-Y., Ho P. T. P., Hwang C.-Y., Shimajiri Y., Matsushita S., Koch P. M., Iono D., 2016, *ApJ*, **831**, 72
 Hsieh P.-Y., Koch P. M., Ho P. T. P., Kim W.-T., Tang Y.-W., Wang H.-H., Yen H.-W., Hwang C.-Y., 2017, *ApJ*, **847**, 3
 Hsieh P.-Y., et al., 2021, *ApJ*, **913**, 94
 Ikeda M., Ohishi M., Nummelin A., Dickens J. E., Bergman P., Hjalmarsen Å., Irvine W. M., 2001, *ApJ*, **560**, 792
 Immer K., Menten K. M., Schuller F., Lis D. C., 2012, *A&A*, **548**, A120
 Immer K., Kauffmann J., Pillai T., Ginsburg A., Menten K. M., 2016, *A&A*, **595**, A94
 Inutsuka S., 2021, in Tsuboi M., Oka T., eds, *Astronomical Society of the Pacific Conference Series Vol. 528, New Horizons in Galactic Center Astronomy and Beyond*. p. 271
 Jimenez-Serra I., 2025, *arXiv e-prints*, p. [arXiv:2501.01782](https://arxiv.org/abs/2501.01782)
 Jimenez-Serra I., Codella C., Belloche A., 2025, *arXiv e-prints*, p. [arXiv:2503.17104](https://arxiv.org/abs/2503.17104)
 Johnston K. G., Beuther H., Linz H., Schmiedeke A., Ragan S. E., Henning T., 2014, *A&A*, **568**, A56
 Jones P. A., Burton M. G., Tothill N. F. H., Cunningham M. R., 2011, *MNRAS*, **411**, 2293
 Jones P. A., et al., 2012, *MNRAS*, **419**, 2961

- Jørgensen J. K., et al., 2016, *A&A*, **595**, A117
- Kauffmann J., Pillai T., Zhang Q., 2013, *ApJ*, **765**, L35
- Koch E., et al., 2025, radio-astro-tools/radio-beam: v0.3.9, doi:10.5281/zenodo.15677957
- Krieger N., et al., 2017, *ApJ*, **850**, 77
- Kruijssen J. M. D., Longmore S. N., 2013, *MNRAS*, **435**, 2598
- Kruijssen J. M. D., Longmore S. N., Elmegreen B. G., Murray N., Bally J., Testi L., Kennicutt R. C., 2014, *MNRAS*, **440**, 3370
- Kruijssen J. M. D., et al., 2019, *MNRAS*, **484**, 5734
- Krumholz M. R., Kruijssen J. M. D., 2015, *MNRAS*, **453**, 739
- Krumholz M. R., Kruijssen J. M. D., Crocker R. M., 2017, *MNRAS*, **466**, 1213
- Lang C. C., Goss W. M., Wood O. S., 1997, *ApJ*, **474**, 275
- Lang C. C., Goss W. M., Morris M., 2002, *AJ*, **124**, 2677
- Li Z.-Y., et al., 2025, *A&A*, **697**, A190
- Lindberg J. E., Aalto S., Costagliola F., Pérez-Beaupuits J.-P., Monje R., Muller S., 2011, *A&A*, **527**, A150
- Lipman D., et al., 2025, *ApJ*, **984**, 159
- Lis D. C., Carlstrom J. E., 1994, *ApJ*, **424**, 189
- Lis D. C., Serabyn E., Zylka R., Li Y., 2001, *ApJ*, **550**, 761
- Liu H. B., Ho P. T. P., Wright M. C. H., Su Y.-N., Hsieh P.-Y., Sun A.-L., Kim S. S., Minh Y. C., 2013, *ApJ*, **770**, 44
- Longmore S., ACES Team 2025, *ApJ*, **1**, 1
- Longmore S. N., et al., 2013, *MNRAS*, **429**, 987
- Lu X., 2025, in prep.
- Lu X., et al., 2017, *ApJ*, **839**, 1
- Lu X., et al., 2019a, *ApJS*, **244**, 35
- Lu X., et al., 2019b, *ApJ*, **872**, 171
- Lu X., et al., 2021, *ApJ*, **909**, 177
- Martín-Pintado J., de Vicente P., Rodríguez-Fernández N. J., Fuente A., Planesas P., 2000, *A&A*, **356**, L5
- Martín S., Martín-Pintado J., Montero-Castaño M., Ho P. T. P., Blundell R., 2012, *A&A*, **539**, A29
- Mehring D. M., Yusef-Zadeh F., Palmer P., Goss W. M., 1992, *ApJ*, **401**, 168
- Mehring D. M., Palmer P., Goss W. M., Yusef-Zadeh F., 1993, *ApJ*, **412**, 684
- Meier D. S., Turner J. L., 2005, *ApJ*, **618**, 259
- Mendoza E., et al., 2018, *MNRAS*, **475**, 5501
- Mills E., Morris M. R., Lang C. C., Dong H., Wang Q. D., Cotera A., Stolovy S. R., 2011, *ApJ*, **735**, 84
- Mills E. A. C., Güsten R., Requena-Torres M. A., Morris M. R., 2013, *ApJ*, **779**, 47
- Miyawaki R., Tsuboi M., Uehara K., Miyazaki A., 2021, *PASJ*, **73**, 943
- Morris M., Serabyn E., 1996, *ARA&A*, **34**, 645
- Oya Y., et al., 2017, *ApJ*, **837**, 174
- Petkova M. A., et al., 2021, arXiv e-prints, p. arXiv:2104.09558
- Pety J., et al., 2017, *A&A*, **599**, A98
- Pickett H. M., Poynter R. L., Cohen E. A., Delitsky M. L., Pearson J. C., Müller H. S. P., 1998, *J. Quant. Spectrosc. Radiative Transfer*, **60**, 883
- Pineau des Forets G., Roueff E., Schilke P., Flower D. R., 1993, *MNRAS*, **262**, 915
- Price-Whelan A. M., et al., 2018, *AJ*, **156**, 123
- Rathborne J. M., et al., 2014, *ApJ*, **795**, L25
- Rathborne J. M., et al., 2015, *ApJ*, **802**, 125
- Requena-Torres M. A., Martín-Pintado J., Rodríguez-Franco A., Martín S., Rodríguez-Fernández N. J., de Vicente P., 2006, *A&A*, **455**, 971
- Requena-Torres M. A., et al., 2012, *A&A*, **542**, L21
- Robitaille T., Bressert E., 2012, APLpy: Astronomical Plotting Library in Python, Astrophysics Source Code Library (ascl:1208.017)
- Rodríguez-Franco A., Martín-Pintado J., Fuente A., 1998, *A&A*, **329**, 1097
- Sault R. J., Teuben P. J., Wright M. C. H., 1995, in Shaw R. A., Payne H. E., Hayes J. J. E., eds, *Astronomical Society of the Pacific Conference Series Vol. 77, Astronomical Data Analysis Software and Systems IV*. p. 433 (arXiv:astro-ph/0612759), doi:10.48550/arXiv.astro-ph/0612759
- Schilke P., Walmsley C. M., Pineau des Forets G., Flower D. R., 1997, *A&A*, **321**, 293
- Schöier F. L., van der Tak F. F. S., van Dishoeck E. F., Black J. H., 2005, *A&A*, **432**, 369
- Simpson J. P., Colgan S. W. J., Cotera A. S., Kaufman M. J., Stolovy S. R., 2018, *ApJ*, **867**, L13
- Simpson J. P., Colgan S. W. J., Cotera A. S., Kaufman M. J., Stolovy S. R., 2021, *ApJ*, **910**, 59
- Sofue Y., et al., 2025, arXiv e-prints, p. arXiv:2506.11553
- Sormani M. C., et al., 2022, *MNRAS*, **512**, 1857
- Steinke M., Oskinova L. M., Hamann W. R., Sander A., Liermann A., Todt H., 2016, *A&A*, **588**, A9
- Suzuki H., Yamamoto S., Ohishi M., Kaifu N., Ishikawa S.-I., Hirahara Y., Takano S., 1992, *ApJ*, **392**, 551
- Tacconi L. J., et al., 2008, *ApJ*, **680**, 246
- Tress R. G., Sormani M. C., Glover S. C. O., Klessen R. S., Battersby C. D., Clark P. C., Hatchfield H. P., Smith R. J., 2020, *MNRAS*, **499**, 4455
- Tsuboi M., Handa T., Ukita N., 1999, *ApJS*, **120**, 1
- Tsuboi M., Miyazaki A., Uehara K., 2015, *PASJ*, **67**, 109
- Tsuboi M., Kitamura Y., Uehara K., Miyazaki A., Miyawaki R., Tsutsumi T., Miyoshi M., 2019, *PASJ*, **71**, 128
- Uehara K., Tsuboi M., Kitamura Y., Miyawaki R., Miyazaki A., 2019, *ApJ*, **872**, 121
- Walker D., ACES Team 2025, *ApJ*, **1**, 1
- Walker D. L., et al., 2021, *MNRAS*, **503**, 77
- Walker D. L., et al., 2025, *ApJ*, **984**, 158
- Walmsley C. M., Winnemisser G., Toelle F., 1980, *A&A*, **81**, 245
- Waskom M. L., 2021, *Journal of Open Source Software*, **6**, 3021
- Yusef-Zadeh F., Wardle M., Lis D., Viti S., Brogan C., Chambers E., Pound M., Rickert M., 2013, *Journal of Physical Chemistry A*, **117**, 9404
- Zeng S., et al., 2020, *MNRAS*, **497**, 4896
- Zhao J.-H., Morris M. R., Goss W. M., An T., 2009, *ApJ*, **699**, 186

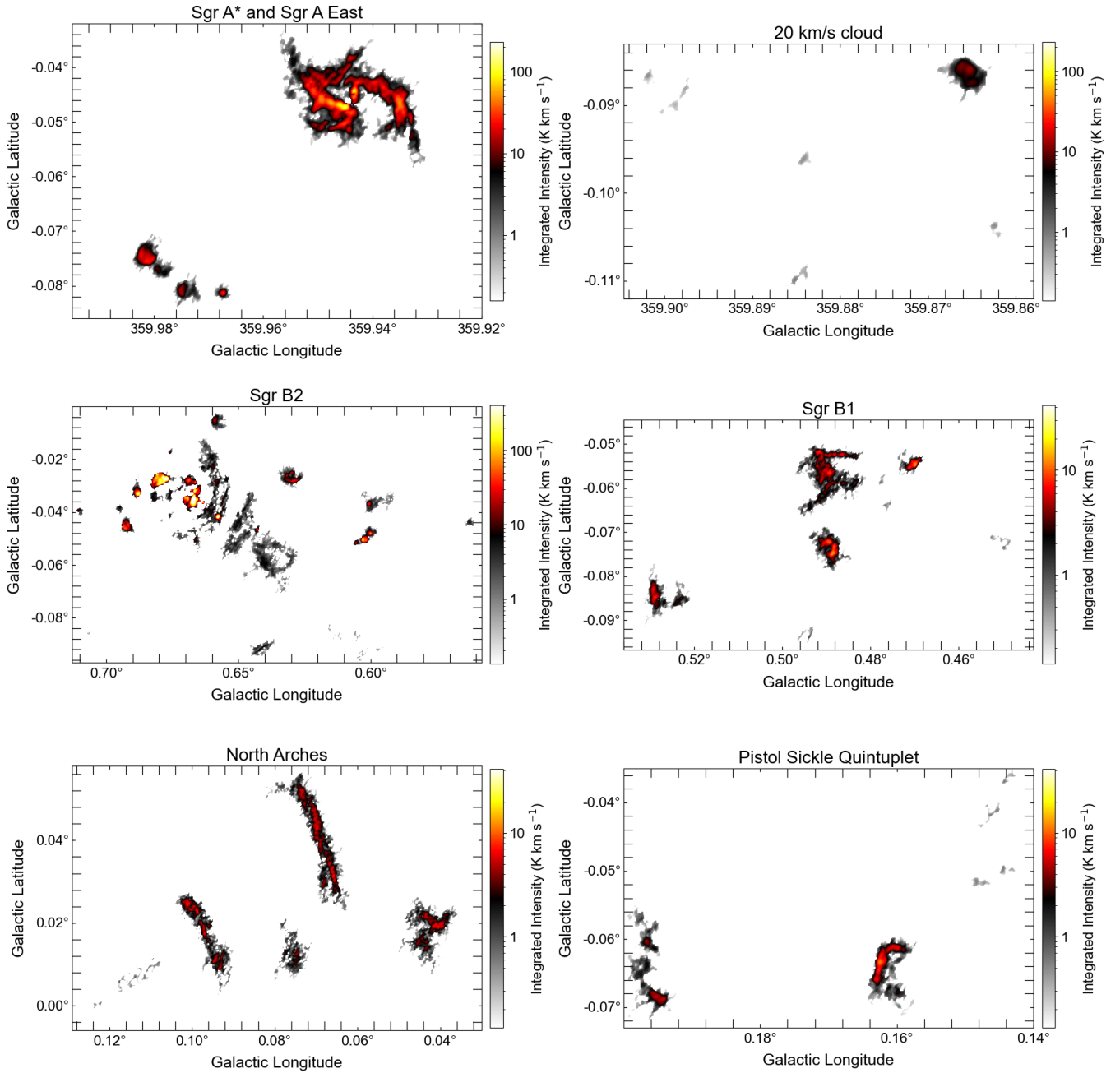
ACES H40 α MOM0

Figure A1. The zoom-in views of the ACES H40 α mom0 images show regions with significant detections. For easy comparison, the names of the regions follow the nomenclature adopted in Ginsburg & ACES Team (2025).

APPENDIX A: ZOOM-INS OF H40 α LINE

The H40 α map indicative of ionized gas associated with the H II regions in the Sgr A mini-spiral (e.g. Zhao et al. 2009) and H II region G-0.02-0.07 (e.g. Ekers et al. 1983; Mills et al. 2011; Uehara et al. 2019), the possible H II region detected in the 20 km s^{-1} cloud (Ho et al. 1985; Lu et al. 2019b), the Sgr B1 (e.g., Mehringer et al. 1992; Simpson et al. 2018, 2021) and Sgr B2 (e.g. Mehringer et al. 1993; De Pree et al. 2011; Jones et al. 2011), the Arched filaments (e.g. Lang et al. 2002), the pistol and sickle (e.g. Lang et al. 1997; Steinke et al. 2016). These sources are significantly detected in the ACES data.

Table B1. DS9 regions in Galactic coordinates. Centers are in degrees; lengths are in arcseconds. For **box**, width/height are full sizes; for **ellipse**, the values are radii. Position angle (PA) in degrees.

Region	Shape	ℓ (deg)	b (deg)	Width/Radius _x (arcsec)	Height/Radius _y (arcsec)	PA (deg)
TLP clouds	box	0.096408	-0.077577	364	129	0
CND	ellipse	359.944183	-0.045176	121	164	68
Brick	box	0.245984	0.011100	175	123	0
20 and 50 km s ⁻¹ cloud	box	359.908	0.-0.0836	675	136	335

APPENDIX B: 2-D CORRELATION MATRIX

In Figure B1, we present the two-dimensional (2D) Pearson correlation coefficients among the 14 lines and the continuum images. A detailed description of the method is provided in Paper IV. The regions used for these calculations are listed in Table B1.

We include the correlation matrices to quantify how the spatial distributions of line intensities vary among different molecular tracers across each CMZ field. Each matrix element represents the normalized covariance between the brightness distributions of two spectral lines, measured over all valid pixels. A high correlation (1) means the lines vary together spatially, tracing similar gas structures or excitation conditions. A low correlation (0) indicates independent spatial variations, while a negative correlation (-1) implies anti-correlated emission. In general, molecular lines correlate strongly with one another, consistent with their tracing of dense gas structures. However, the overall correlation strength differs across regions: correlations are highest in the TLP, indicating that most molecular tracers vary together spatially, whereas the CND exhibits the lowest correlations. The weaker correlations in the CND suggest that the emission arises from multiple, physically distinct components along the line of sight, leading to less coherent spatial correspondence between tracers. This highlights the increased structural and chemical complexity near Sgr A* compared to regions farther out in the CMZ. We note that the similarity analysis presented in this paper provides a first-order comparison. A more detailed analysis, selecting specific regions or structures, is essential to derive more accurate values.

APPENDIX C: DATA RELEASE SUMMARY

The data products from the ACES survey follow a uniform naming convention. The filenames for the data products presented in this paper can be constructed using the templates described below, in conjunction with the information provided in Appendix A of Walker & ACES Team (2025).

The following subsections are divided according to different product types which occur at the Member ObsUnitSet (MOUS) and Group ObsUnitSet (GOUS) levels².

C1 Member-level products (12m and 7m)

We release the data cubes for all SPWs for the 45 ACES regions. These are member-level products, and correspond to the cubes for the 12m and 7m arrays for each field prior to combination.

We release the cubes for the separate arrays as they are different to those initially delivered by ALMA due to the changes that were made during reprocessing. We do not re-release any of the stand-alone TP products, as we used the same cubes as those available in the ALMA Science Archive (ASA).

In this and subsequent subsections, we describe how to construct the filenames of the released data products by providing filename templates that include placeholder variables. These placeholders can be changed as needed to build the filename of the relevant product.

Following the requirements of the ASA, the filename template is:

```
member.uid__A001_{mous-id}.lp_slongmore.{field_coords}.{array}.{frqrange}.cube.pbcor.fits
```

The placeholder template components should be replaced as follows:

- **{mous-id}**: The 12m or 7m MOUS ID for a given field, as listed in Table A1 in Walker & ACES Team (2025).
- **{field_coords}**: The central coordinates of the field, as listed in Table A1 in Walker & ACES Team (2025) (e.g., G000.073+0.184).
- **{array}**: The ALMA array, either 12m or 7m.
- **{frqrange}**: The frequency range, which depends on the SPW:
 - SPW 33: 97.7–99.5GHz
 - SPW 35: 99.6–101.4GHz

For example, to find the 12m-only cube for CS for field ao (this field contains the well-known molecular cloud G0.253+0.016, aka the Brick), the resulting filename would be:

```
member.uid__A001_X15a0_X190.lp_slongmore.G000.300+0.063.12m.97.7-99.5GHz.cube.pbcor.fits
```

² For a description of ALMA project structures and naming conventions, please refer to Section 2 of the Cycle 9 QA2 guide: <https://almascience.eso.org/documents-and-tools/cycle9/alma-qa2-data-products-for-cycle-9>

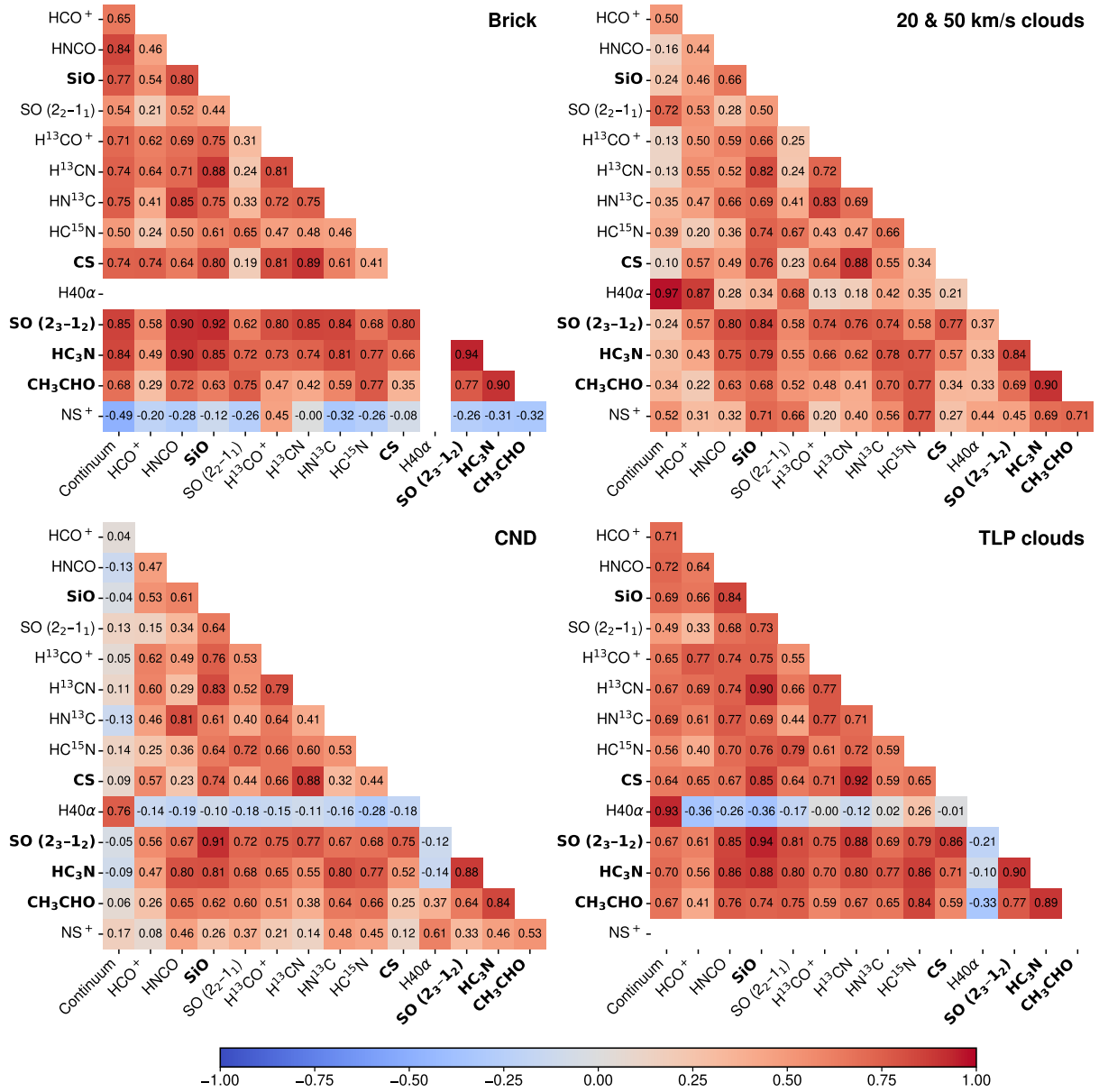


Figure B1. 2-D correlation matrix between the continuum and integrated intensities (mom 0 images) of the spectral lines presented in this paper, Paper III, and Paper IV. In the Figure 12 of Paper IV, all the pixels in the ACES mosaic fields are considered. In this paper we present the sub-fields towards the Brick cloud, the 20 and 50 km s⁻¹ clouds, and CND, the TLP clouds, the Sgr C and Sgr B regions. Note that the Sgr A* is excluded in the CND region. The Sgr A* is centered on $(l, b) = (359.944^\circ, -0.046^\circ)$, with a radius of 4.2". Negative values mean anti-correlation, and the blank cells mean the invalid values in the images preventing calculation.

C2 Group-level products (Combined cubes per region)

We also release array-combined products per SPW per region. As these products combine data from multiple MOUSs, they are deemed to be group-level products. The filenames of these products can be constructed as follows:

```
group.uid___A001_X1590_X30a9.lp_slongmore.{field_coords}.{arrays}.{frqrange}.cube.pbcor.fits
```

Where the template components are:

- **{field_coords}** and **{frqrange}**: follow the same definition as for the member-level products.
- **{arrays}**: 12m7mTP

As an example, the corresponding CS cube including 12m, 7m, and TP data for field ao would be:

```
group.uid___A001_X1590_X30a9.lp_slongmore.G000.300+0.063.12m7mTP.97.7-99.5GHz.cube.pbcor.fits
```

C3 Group-level products (Full CMZ mosaics)

Finally, we release the full, contiguous mosaics covering the entire ACES footprint. Again, since these result from the combination of many MOUSs, the full mosaics are at the group level.

In contrast to cubes for the individual fields, we do not release full mosaics for all SPWs, but rather for specific lines. The lines relevant to this paper are given in Table 1. Most of the SPWs are sufficiently broad that they contain significant spectral ranges with no line emission. We therefore opted to not produce full mosaics containing these blank channels in the interest of reducing the file sizes. In addition to the data cubes for each line, we also release a suite of advanced products, including moment maps, noise maps, etc. (see below).

The filename template for the full mosaic cubes and associated products is:

`group.uid__A001_X1590_X30a9.lp_slongmore.cmz_mosaic.{arrays}.{molecule}.{suffix}`

Where the template components are:

- `{arrays}`: 12m7mTP
- `{molecule}`: HC3N, CS21, H40a, CH3CHO, S032
- `{suffix}` defines the specific data product. Products released with this paper are:
 - `cube.pbcor.fits`: primary beam corrected image cube.
 - `cube.downsampled_spatially.pbcor.fits`: as previous, spatially smoothed to a 5 arcsec beam and then spatially rebinned by a factor of 9×9 .
 - `integrated_intensity.fits`: masked integrated intensity map of the full-resolution cube.
 - `mad_std.fits`: noise map of the full-resolution cube.
 - `peak_intensity.fits`: peak intensity map of the full-resolution cube.
 - `velocity_at_peak_intensity.fits`: velocity map from the masked full-resolution cube; velocity estimated using the peak intensity of the spectrum for each pixel.
 - `PV_l_max.fits`: ℓ - v position-velocity map from the full-resolution cube; maximum intensity taken along Galactic latitude (b).
 - `PV_l_mean.fits`: ℓ - v position-velocity map from the masked full-resolution cube; mean intensity taken along Galactic latitude (b).
 - `PV_b_max.fits`: b - v position-velocity map from the full-resolution cube; maximum intensity taken along Galactic longitude (ℓ).
 - `PV_b_mean.fits`: b - v position-velocity map from the full-resolution cube; mean intensity taken along Galactic longitude (ℓ).

Table C1. Global statistics for SPW 33 and SPW 35 cubes for all ACES regions, with velocity offset V_{off} added as the second column.

Field	V_{off} (km s^{-1})	SPW _{12m}	B_{maj} (")	B_{min} (")	BPA (deg)	Image size (pix)	No. channels	Pixel size (")	S_{peak} (mJy beam^{-1})	σ_{MAD} (mJy beam^{-1})
a	40	33	1.49	1.10	-67.0	(2070, 2482)	3840.0	0.20	128.3	3.9
a	40	35	1.42	1.06	-66.0	(2070, 2482)	3840.0	0.20	112.5	3.6
aa	0	33	1.63	1.44	-52.0	(1593, 1456)	3839.0	0.26	372.5	3.7
aa	0	35	1.63	1.41	-52.0	(1593, 1456)	3839.0	0.26	298.2	3.4
ab	0	33	1.63	1.52	-75.0	(1465, 1236)	3836.0	0.28	199.7	3.6
ab	0	35	1.60	1.48	-75.0	(1465, 1236)	3836.0	0.28	179.7	3.3
ac	0	33	1.54	1.06	-71.0	(1638, 1601)	3840.0	0.19	166.4	4.3
ac	0	35	1.51	1.03	-71.0	(1638, 1601)	3840.0	0.19	145.7	4.0
ad	0	33	1.79	1.78	-75.0	(1140, 2527)	3840.0	0.20	221.4	4.3
ad	0	35	1.77	1.75	-75.0	(1140, 2527)	3840.0	0.20	203.2	4.0
ae	0	33	1.88	1.52	83.0	(1313, 1344)	3840.0	0.30	253.0	3.8
ae	0	35	1.87	1.51	83.0	(1313, 1344)	3840.0	0.30	238.1	3.5
af	0	33	2.50	1.74	86.0	(1417, 1165)	3840.0	0.31	509.2	3.9
af	0	35	2.44	1.71	86.0	(1417, 1165)	3840.0	0.31	487.0	3.7
ag	0	33	1.65	1.26	-70.0	(1698, 1696)	3840.0	0.24	149.7	4.2
ag	0	35	1.62	1.24	-70.0	(1698, 1696)	3840.0	0.24	141.2	4.0
ah	30	33	1.66	1.12	-61.0	(1957, 1936)	3840.0	0.20	200.0	3.5
ah	30	35	1.64	1.09	-61.0	(1957, 1936)	3840.0	0.20	188.7	3.3
ai	0	33	2.11	1.52	79.0	(1350, 1601)	3840.0	0.29	285.0	3.7
ai	0	35	2.06	1.49	79.0	(1350, 1601)	3840.0	0.29	260.8	3.4
aj	-30	33	1.85	1.47	86.0	(1414, 1265)	3836.0	0.31	492.7	3.8
aj	-30	35	1.83	1.45	86.0	(1414, 1265)	3836.0	0.31	462.5	3.6
ak	30	33	1.96	1.67	80.0	(736, 988)	3836.0	0.32	256.3	3.8
ak	30	35	1.92	1.64	80.0	(736, 988)	3836.0	0.32	243.7	3.6
al	0	33	2.37	1.79	86.0	(2167, 1422)	3840.0	0.28	217.8	4.4
al	0	35	2.30	1.76	86.0	(2167, 1422)	3840.0	0.28	205.3	4.1
am	30	33	2.84	1.92	89.0	(2578, 1117)	3840.0	0.30	5064.8	4.9
am	30	35	2.79	1.90	89.0	(2578, 1117)	3840.0	0.30	4820.0	4.5
an	30	33	2.31	1.67	83.0	(1305, 1336)	3840.0	0.30	333.8	4.0
an	30	35	2.28	1.65	83.0	(1305, 1336)	3840.0	0.30	312.7	3.7
ao	0	33	2.28	1.58	-86.0	(2481, 897)	3839.0	0.28	320.8	5.1
ao	0	35	2.25	1.56	-86.0	(2481, 897)	3839.0	0.28	308.6	4.7
ap	0	33	1.88	1.53	79.0	(1314, 1347)	3836.0	0.30	469.7	3.5
ap	0	35	1.86	1.51	79.0	(1314, 1347)	3836.0	0.30	452.2	3.2
aq	0	33	1.62	1.34	-78.0	(1785, 1787)	3840.0	0.22	370.2	3.8
aq	0	35	1.60	1.32	-78.0	(1785, 1787)	3840.0	0.22	349.1	3.5
ar	40	33	2.13	2.11	85.0	(1355, 1401)	3840.0	0.29	348.7	4.2
ar	40	35	2.10	2.08	85.0	(1355, 1401)	3840.0	0.29	336.9	3.9
as	0	33	1.77	1.23	-69.0	(1965, 2020)	3837.0	0.20	308.4	4.1
as	0	35	1.75	1.21	-69.0	(1965, 2020)	3837.0	0.20	296.6	3.7
b	40	33	1.57	1.55	87.0	(1872, 1925)	3813.0	0.21	2100.5	3.2
b	40	35	1.53	1.52	87.0	(1872, 1925)	3813.0	0.21	2043.2	2.9
c	0	33	2.53	1.74	85.0	(1404, 1436)	3839.0	0.28	329.7	4.4
c	0	35	2.50	1.72	85.0	(1404, 1436)	3839.0	0.28	308.9	4.1
d	30	33	1.72	1.39	-60.0	(2022, 1556)	3839.0	0.23	156.4	4.1
d	30	35	1.69	1.37	-60.0	(2022, 1556)	3839.0	0.23	145.1	3.8
e	-30	33	2.19	1.50	83.0	(1410, 1446)	3839.0	0.28	273.6	4.6
e	-30	35	2.14	1.48	83.0	(1410, 1446)	3839.0	0.28	260.0	4.3
f	0	33	2.20	1.32	87.0	(1750, 1442)	3840.0	0.28	353.3	4.5
f	0	35	2.18	1.30	87.0	(1750, 1442)	3840.0	0.28	341.0	4.2
g	30	33	1.72	1.35	-85.0	(1572, 1619)	3840.0	0.25	198.8	4.1
g	30	35	1.68	1.32	-85.0	(1572, 1619)	3840.0	0.25	187.0	3.8
h	0	33	1.46	1.13	-78.0	(1951, 2083)	3840.0	0.21	173.2	3.9
h	0	35	1.42	1.10	-78.0	(1951, 2083)	3840.0	0.21	160.9	3.6
i	30	33	1.47	1.27	-59.0	(1646, 1613)	3832.0	0.25	260.0	3.5
i	30	35	1.43	1.23	-59.0	(1646, 1613)	3832.0	0.25	243.5	3.2

Table C1 – continued

Field	V_{off} (km s^{-1})	SPW _{12m}	B_{maj} (")	B_{min} (")	BPA (deg)	Image size (pix)	No. channels	Pixel size (")	S_{peak} (mJy beam^{-1})	σ_{MAD} (mJy beam^{-1})
j	30	33	2.21	1.26	-87.0	(1446, 1485)	3819.0	0.27	317.1	4.6
j	30	35	2.17	1.24	-87.0	(1446, 1485)	3819.0	0.27	301.0	4.3
k	30	33	1.63	1.01	-75.0	(2174, 2167)	3832.0	0.18	140.8	4.3
k	30	35	1.60	0.99	-75.0	(2174, 2167)	3832.0	0.18	130.7	4.0
l	0	33	1.64	1.52	-51.0	(2383, 1497)	3840.0	0.26	851.0	4.1
l	0	35	1.61	1.50	-51.0	(2383, 1497)	3840.0	0.26	823.6	3.8
m	30	33	2.22	1.85	81.0	(1345, 1356)	3840.0	0.29	2975.0	3.5
m	30	35	2.18	1.82	81.0	(1345, 1356)	3840.0	0.29	2850.0	3.2
n	30	33	2.62	1.28	75.0	(1366, 1823)	3840.0	0.19	231.5	5.3
n	30	35	2.60	1.25	75.0	(1366, 1823)	3840.0	0.19	218.4	4.9
o	0	33	2.04	1.56	83.0	(1281, 1230)	3835.0	0.32	378.3	4.4
o	0	35	2.00	1.53	83.0	(1281, 1230)	3835.0	0.32	359.2	4.1
p	0	33	1.58	1.26	89.0	(1856, 1839)	3836.0	0.22	270.7	3.7
p	0	35	1.54	1.23	89.0	(1856, 1839)	3836.0	0.22	255.0	3.4
q	0	33	2.02	1.55	88.0	(1315, 1343)	3836.0	0.30	279.5	3.3
q	0	35	1.99	1.53	88.0	(1315, 1343)	3836.0	0.30	262.0	3.1
r	30	33	2.34	1.36	-86.0	(1535, 1395)	3840.0	0.29	344.4	4.4
r	30	35	2.30	1.33	-86.0	(1535, 1395)	3840.0	0.29	327.0	4.1
s	0	33	2.53	1.97	80.0	(1310, 1346)	3839.0	0.30	618.6	3.8
s	0	35	2.48	1.94	80.0	(1310, 1346)	3839.0	0.30	593.7	3.5
t	0	33	2.15	1.95	65.0	(1269, 1273)	3840.0	0.31	327.7	3.9
t	0	35	2.11	1.91	65.0	(1269, 1273)	3840.0	0.31	310.8	3.6
u	30	33	1.71	1.18	-67.0	(1347, 2051)	3834.0	0.19	139.5	4.5
u	30	35	1.68	1.15	-67.0	(1347, 2051)	3834.0	0.19	130.2	4.2
v	30	33	1.60	1.02	-79.0	(1362, 1880)	3819.0	0.19	236.6	4.2
v	30	35	1.58	1.00	-79.0	(1362, 1880)	3819.0	0.19	220.5	3.9
w	30	33	2.01	1.42	-79.0	(1474, 1399)	3819.0	0.28	199.0	3.4
w	30	35	1.98	1.39	-79.0	(1474, 1399)	3819.0	0.28	189.2	3.2
x	0	33	2.20	1.49	-86.0	(1291, 769)	3836.0	0.30	396.7	4.2
x	0	35	2.17	1.46	-86.0	(1291, 769)	3836.0	0.30	377.1	3.9
y	0	33	1.86	1.37	-85.0	(1428, 1112)	3835.0	0.27	209.9	4.3
y	0	35	1.83	1.34	-85.0	(1428, 1112)	3835.0	0.27	198.2	4.0
z	40	33	1.96	1.28	79.0	(1350, 1353)	3813.0	0.29	153.1	4.3
z	40	35	1.92	1.25	79.0	(1350, 1353)	3813.0	0.29	142.7	4.0

AUTHOR AFFILIATIONS

- ¹National Astronomical Observatory of Japan, 2-21-1 Osawa, Mitaka, Tokyo 181-8588, Japan
- ²UK ALMA Regional Centre Node, Jodrell Bank Centre for Astrophysics, The University of Manchester, Manchester M13 9PL, UK
- ³Department of Astronomy, University of Florida, P.O. Box 112055, Gainesville, FL 32611, USA
- ⁴European Southern Observatory (ESO), Karl-Schwarzschild-Straße 2, 85748 Garching, Germany
- ⁵Shanghai Astronomical Observatory, Chinese Academy of Sciences, 80 Nandan Road, Shanghai 200030, P. R. China
- ⁶State Key Laboratory of Radio Astronomy and Technology, A20 Datun Road, Chaoyang District, Beijing, 100101, P. R. China
- ⁷Institut de Ciències de l’Espai (ICE), CSIC, Campus UAB, Carrer de Can Magrans s/n, E-08193, Bellaterra, Barcelona, Spain
- ⁸Institut d’Estudis Espacials de Catalunya (IEEC), E-08860, Castelldefels, Barcelona, Spain
- ⁹University of Maryland, Department of Astronomy, College Park, MD 20742-2421, USA
- ¹⁰Max-Planck-Institut für extraterrestrische Physik, Gießenbachstraße 1, 85748 Garching bei München, Germany
- ¹¹Department of Physics and Astronomy, University of Kansas, 1251 Wescoe Hall Drive, Lawrence, KS 66045, USA
- ¹²Astrophysics Research Institute, Liverpool John Moores University, 146 Brownlow Hill, Liverpool L3 5RF, The UK
- ¹³Max Planck Institute for Astronomy, Königstuhl 17, D-69117 Heidelberg, Germany
- ¹⁴Astronomisches Rechen-Institut, Zentrum für Astronomie der Universität Heidelberg, Mönchhofstraße 12-14, D-69120 Heidelberg, Germany
- ¹⁵Cosmic Origins Of Life (COOL) Research DAO, <https://coolresearch.io>
- ¹⁶European Southern Observatory, Alonso de Córdova, 3107, Vitacura, Santiago 763-0355, Chile
- ¹⁷Joint ALMA Observatory, Alonso de Córdova, 3107, Vitacura, Santiago 763-0355, Chile
- ¹⁸School of Astronomy and Space Science, Nanjing University, 163 Xianlin Avenue, Nanjing 210023, P.R.China
- ¹⁹Key Laboratory of Modern Astronomy and Astrophysics (Nanjing University), Ministry of Education, Nanjing 210023, P.R.China
- ²⁰Center for Astrophysics | Harvard & Smithsonian, 60 Garden Street, Cambridge, MA 02138, USA
- ²¹Haystack Observatory, Massachusetts Institute of Technology, 99 Millstone Road, Westford, MA 01886, USA
- ²²Center for Astrophysics and Space Astronomy, Department of Astrophysical and Planetary Sciences, University of Colorado, Boulder, CO 80389, USA
- ²³Department of Physics, University of Connecticut, 196A Auditorium Road, Unit 3046, Storrs, CT 06269, USA
- ²⁴Centro de Astrobiología (CAB), CSIC-INTA, Carretera de Ajalvir km 4, 28850 Torrejón de Ardoz, Madrid, Spain
- ²⁵Academia Sinica Institute of Astronomy and Astrophysics, Astronomy-Mathematics Building, AS/NTU No.1, Sec. 4, Roosevelt Rd, Taipei 10617, Taiwan
- ²⁶Space, Earth and Environment Department, Chalmers University of Technology, SE-412 96 Gothenburg, Sweden
- ²⁷Como Lake centre for AstroPhysics (CLAP), DiSAT, Università dell’Insubria, via Valleggio 11, 22100 Como, Italy
- ²⁸Institute of Physics, Laboratory for Galaxy Evolution and Spectral Modelling, EPFL, Observatoire de Sauverny, Chemin Pegasi 51, 1290 Versoix, Switzerland
- ²⁹Observatorio Astronómico de Quito, Observatorio Astronómico Nacional, Escuela Politécnica Nacional, 170403, Quito, Ecuador
- ³⁰INAF Arcetri Astrophysical Observatory, Largo Enrico Fermi 5, Firenze, 50125, Italy
- ³¹Jodrell Bank Centre for Astrophysics, The University of Manchester, Manchester M13 9PL, UK
- ³²National Radio Astronomy Observatory, 520 Edgemont Road, Charlottesville, VA 22903, USA
- ³³Universität Heidelberg, Zentrum für Astronomie, Institut für Theoretische Astrophysik, Albert-Ueberle-Str 2, D-69120 Heidelberg, Germany
- ³⁴Research School of Astronomy and Astrophysics, Australian National University, Canberra, ACT 2611, Australia
- ³⁵Instituto de Astrofísica de Andalucía, CSIC, Glorieta de la Astronomía s/n, 18008 Granada, Spain
- ³⁶Instituto de Astronomía, Universidad Católica del Norte, Av. Angamos 0610, Antofagasta, Chile
- ³⁷Chinese Academy of Sciences South America Center for Astronomy, National Astronomical Observatories, CAS, Beijing 100101, China
- ³⁸Institute for Advanced Study, 1 Einstein Drive, Princeton, NJ 08540, USA
- ³⁹Department of Physics and Astronomy, University College London, Gower Street, London WC1E 6BT, UK
- ⁴⁰Universität Heidelberg, Interdisziplinäres Zentrum für Wissenschaftliches Rechnen, Im Neuenheimer Feld 225, 69120 Heidelberg, Germany
- ⁴¹Elizabeth S. and Richard M. Cashin Fellow at the Radcliffe Institute for Advanced Studies at Harvard University, 10 Garden Street, Cambridge, MA 02138, U.S.A.
- ⁴²Institute for Research in Fundamental Sciences (IPM), School of Astronomy, Tehran, Iran
- ⁴³Department of Physics, Villanova University, 800 E. Lancaster Ave., Villanova, PA 19085, USA
- ⁴⁴Departamento de Astronomía, Universidad de La Serena, Raúl Bitrán 1305, La Serena, Chile
- ⁴⁵Instituto de Física Fundamental (CSIC), Calle Serrano 121-123, 28006, Madrid, Spain
- ⁴⁶Green Bank Observatory, P.O. Box 2, Green Bank, WV 24944, USA
- ⁴⁷Institute of Astronomy, The University of Tokyo, Mitaka, Tokyo 181-0015, Japan
- ⁴⁸Department of Astronomy, University of Massachusetts, Amherst, MA 01003, USA
- ⁴⁹Department of Physics, Aberystwyth University, Ceredigion, Cymru, SY23 3BZ, UK
- ⁵⁰Kavli Institute for Astronomy and Astrophysics, Peking University, Beijing 100871, People’s Republic of China
- ⁵¹Department of Astronomy, School of Physics, Peking University, Beijing, 100871, People’s Republic of China

This paper has been typeset from a $\text{\TeX}/\text{\LaTeX}$ file prepared by the author.